

Berkeley Supernova Ia Program I: Observations, Data Reduction, and Spectroscopic Sample of 582 Low-Redshift Type Ia Supernovae

Jeffrey M. Silverman,^{1,2} Ryan J. Foley,^{3,4} Alexei V. Filippenko,¹
Mohan Ganeshalingam,¹ Aaron J. Barth,⁵ Ryan Chornock,³ Christopher V. Griffith,^{1,6}
Jason J. Kong,¹ Nicholas Lee,⁷ Douglas C. Leonard,⁸ Thomas Matheson,⁹
Emily G. Miller,¹⁰ Thea N. Steele,^{1,11} Brian J. Barris,⁷ Joshua S. Bloom,¹
Bethany E. Cobb,¹² Alison L. Coil,¹³ Louis-Benoit Desroches,^{1,14} Elinor L. Gates,¹⁵
Luis C. Ho,¹⁶ Saurabh W. Jha,¹⁷ Michael T. Kandrashoff,¹ Weidong Li,^{1†}
Kaisey S. Mandel,³ Maryam Modjaz,^{1,18} Matthew R. Moore,¹ Robin E. Mostardi,^{1,19}
Marina S. Papenkova,²⁰ Sung Park,¹ Daniel A. Perley,^{1,21} Dovi Poznanski,^{1,22}
Cassie A. Reuter,^{1,23} James Scala,¹ Franklin J. D. Serduke,¹ Joseph C. Shields,²⁴
Brandon J. Swift,²⁵ John L. Tonry,⁷ Schuyler D. Van Dyk,²⁶ Xiaofeng Wang,²⁷
Diane S. Wong¹

¹Department of Astronomy, University of California, Berkeley, CA 94720-3411, USA

²Marc J. Staley Fellow; email JSilverman@astro.berkeley.edu

³Harvard-Smithsonian Center for Astrophysics, 60 Garden Street, Cambridge, MA 02138, USA

⁴Clay Fellow

⁵Department of Physics and Astronomy, 4129 Frederick Reines Hall, University of California, Irvine, CA 92697, USA

⁶Department of Astronomy and Astrophysics, The Pennsylvania State University, University Park, PA 16802, USA

⁷Institute for Astronomy, University of Hawaii, 2680 Woodlawn Drive, Honolulu, HI 96822, USA

⁸Department of Astronomy, San Diego State University, San Diego, CA 92182-1221, USA

⁹National Optical Astronomy Observatory, 950 North Cherry Avenue, Tucson, AZ 85719-4933, USA

¹⁰University of Pennsylvania, 3451 Walnut Street, Philadelphia, PA 19104, USA

¹¹Department of Computer Science, Kutztown University of Pennsylvania, Kutztown, Pennsylvania 19530, USA

¹²Department of Physics, The George Washington University, Washington, DC 20052, USA

¹³Department of Physics, University of California, San Diego, 9500 Gilman Drive, La Jolla, CA 92093, USA

¹⁴Lawrence Berkeley National Laboratory, 1 Cyclotron Road, Berkeley, CA 94720, USA

¹⁵University of California Observatories/Lick Observatory, P.O. Box 85, Mount Hamilton, CA 95140, USA

¹⁶The Observatories of the Carnegie Institution for Science, 813 Santa Barbara Street, Pasadena, CA 91101, USA

¹⁷Department of Physics and Astronomy, Rutgers the State University of New Jersey, 136 Frelinghuysen Road, Piscataway, NJ 08854, USA

¹⁸Center for Cosmology and Particle Physics, New York University, 4 Washington Place, New York, NY 10003, USA

¹⁹Department of Physics and Astronomy, University of California, Los Angeles, CA 90095, USA

²⁰Department of Physics and Astronomy, East Los Angeles College, Monterey Park, CA 91754, USA

²¹Cahill Center for Astrophysics, California Institute of Technology, Pasadena, CA 91125, USA

²²School of Physics and Astronomy, Tel-Aviv University, Tel Aviv 69978, Israel

²³Department of Physics, Purdue University, West Lafayette, IN 47907-2036, USA

²⁴Department of Physics and Astronomy, Ohio University, Athens, OH 45701, USA

²⁵Steward Observatory, University of Arizona, 933 North Cherry Avenue, Tucson, AZ 85721-0065, USA

²⁶Spitzer Science Center, California Institute of Technology, 1200 East California Boulevard, Pasadena, CA 91125, USA

²⁷Department of Physics and Tsinghua Center for Astrophysics, Tsinghua University, Beijing 100084, China

†Deceased 12 December 2011

ABSTRACT

In this first paper in a series we present 1298 low-redshift ($z \lesssim 0.2$) optical spectra of 582 Type Ia supernovae (SNe Ia) observed from 1989 through 2008 as part of the Berkeley SN Ia Program (BSNIP). 584 spectra of 199 SNe Ia have well-calibrated light curves with measured distance moduli, and many of the spectra have been corrected for host-galaxy contamination. Most of the data were obtained using the Kast double spectrograph mounted on the Shane 3 m telescope at Lick Observatory and have a typical wavelength range of 3300–10,400 Å, roughly twice as wide as spectra from most previously published datasets. We present our observing and reduction procedures, and we describe the resulting SN Database (SNDB), which will be an online, public, searchable database containing all of our fully reduced spectra and companion photometry. In addition, we discuss our spectral classification scheme (using the SuperNova IDentification code, SNID; Blondin & Tonry 2007), utilising our newly constructed set of SNID spectral templates. These templates allow us to accurately classify our entire dataset, and by doing so we are able to reclassify a handful of objects as bona fide SNe Ia and a few other objects as members of some of the peculiar SN Ia subtypes. In fact, our dataset includes spectra of nearly 90 spectroscopically peculiar SNe Ia. We also present spectroscopic host-galaxy redshifts of some SNe Ia where these values were previously unknown. The sheer size of the BSNIP dataset and the consistency of our observation and reduction methods makes this sample unique among all other published SN Ia datasets and is complementary in many ways to the large, low-redshift SN Ia spectra presented by Matheson et al. 2008 and Blondin et al. 2012. In other BSNIP papers in this series, we use these data to examine the relationships between spectroscopic characteristics and various observables such as photometric and host-galaxy properties.

Key words: cosmology: observations – distance scale – supernovae: general – surveys

1 INTRODUCTION

Supernovae (SNe) have been integral to our understanding of the cosmos throughout the history of astronomy — from demonstrating that the sky was not unchanging beyond the lunar sphere (Brahe 1573) to the discovery of the acceleration of the expansion of the Universe (Riess et al. 1998; Perlmutter et al. 1999). Type Ia supernovae (SNe Ia) have been particularly useful in recent years as a way to accurately measure cosmological parameters (Astier et al. 2006; Riess et al. 2007; Wood-Vasey et al. 2007; Hicken et al. 2009; Kessler et al. 2009; Amanullah et al. 2010; Conley et al. 2011; Sullivan et al. 2011; Suzuki et al. 2012). Broadly speaking, SNe Ia are the result of thermonuclear explosions of carbon/oxygen white dwarfs (WDs) (e.g., Hoyle & Fowler 1960; Colgate & McKee 1969; Nomoto et al. 1984; see Hillebrandt & Niemeyer 2000 for a review). However, we still lack a detailed understanding of the progenitor systems and explosion mechanisms, as well as how differences in initial conditions create the variance in observed properties of SNe Ia. To solve these problems, and others, detailed and self-consistent observations of many hundreds of SNe Ia are required.

The cosmological application of SNe Ia as precise distance indicators relies on being able to standardise their luminosity. Phillips (1993) showed that light-curve decline is well correlated with luminosity at peak brightness for most SNe Ia, the so-called “Phillips relation.” Optical colours have also been used to better standardise the luminosity of SNe Ia (e.g., Riess et al. 1996; Tripp 1998). Additionally, people have searched for another, spectroscopic parameter in SN observations which would make our measurements of the distances to SNe Ia even more precise. Bailey et al. (2009)

and Blondin et al. (2011) have decreased the scatter in residuals to the Hubble diagram with the help of optical spectra. Wang et al. (2009) obtained an additional improvement by separating their sample of SNe Ia into two groups based on the ejecta velocity near maximum brightness; they suggested different reddening laws for these two samples. Building on this work, Foley & Kasen (2011) found that the *intrinsic* maximum-light colour of SNe Ia depends on their ejecta velocity. After accounting for this colour difference, the scatter in Hubble-diagram residuals is decreased from 0.19 mag to 0.13 mag for a subset of SNe Ia. This particular conclusion was possible only with a large set of spectroscopically observed objects, with many of the spectra coming from the sample described in this Paper (see also Wang et al. 2009).

Until now there have been several statistical samples of low-redshift SN Ia photometry (e.g., Hamuy et al. 1996; Riess et al. 1999; Jha et al. 2006; Hicken et al. 2009; Ganeshalingam et al. 2010; Contreras et al. 2010; Stritzinger et al. 2011), but only one large sample of low-redshift SN Ia spectra (Matheson et al. 2008). Until the publication of over 432 spectra of 32 SNe Ia by Matheson et al. (2008), large samples of SN Ia spectra were typically constructed by combining datasets published for individual objects, usually from many different groups.

The Berkeley Supernova Ia Program (BSNIP) is a large-scale effort to measure the properties of low-redshift ($z \lesssim 0.2$) SNe Ia, focusing on optical spectroscopy and photometry (see Ganeshalingam et al. 2010, for the companion photometry paper to much of the spectroscopic sample presented here). One aspect of our strategy for the last two decades has been to observe as many SNe Ia as possi-

ble in order to dramatically increase the number of objects with spectroscopic data. We have also attempted to obtain good temporal spectral coverage of peculiar objects as well as objects which were being observed photometrically by our group. In addition, we strove to spectroscopically classify all SNe discovered by the 0.76 m Katzman Automatic Imaging Telescope (KAIT; Filippenko et al. 2001). By observing and reducing our spectra in a consistent manner, we avoid many of the systematic differences found in previous samples constructed from data obtained by various groups.

In this paper we present the low-redshift SN Ia spectral dataset; more details are given by (Silverman 2012). This sample consists of a total of 1298 spectra of 582 SNe Ia observed from 1989 through the end of 2008. A subset of the SNe, along with information about their host galaxies, is presented in Table 1 (the full set is available online — see the Supporting Information). Information regarding some of the SN Ia spectra in the dataset is listed in Table 2 (and again the full set is available online — see the Supporting Information). Many spectra presented in this paper have complementary light curves from Hamuy et al. (1996), Riess et al. (1999), Jha et al. (2006), Hicken et al. (2009), and Ganeshalingam et al. (2010), which have all been compiled and fit by Ganeshalingam et al. (in prep.). Other spectra have complementary unfiltered light curves given by Wang et al. (in prep.).

In this paper, we describe our observations and data-reduction procedure in Sections 2 and 3, respectively. We present our methods of data management and storage in Section 4 and our spectral classification scheme in Section 5. The sample of objects and spectra is described in Section 6, and there we also show our fully reduced spectra as well as (for the objects with multi-band SN and galaxy photometry) galaxy-subtracted spectra. Reclassifications of a handful of SNe, and previously unknown spectroscopic host-galaxy redshifts, are also given. We discuss our conclusions in Section 7. Future BSNIP papers will examine the correlations between spectroscopic properties and other observables (such as photometry and host-galaxy properties).

Table 1: SN Ia and Host Information

SN Name	SNID (Sub)Type ^a	Host Galaxy	Host Morp. ^b	cz_{helio} (km s ⁻¹) ^c	$E(B - V)_{\text{MW}}$ (mag) ^d	Discovery Date (UT)	Discovery Reference	Classification Reference	# of Spec.	First Epoch ^e	Last Epoch ^e	JD _{max} Ref. f
SN 1989A	Ia-norm	NGC 3687	Sbc	2506	0.020	1989-01-19	LAUC 4721	LAUC 4724	1	83.80
SN 1989B	Ia-norm	NGC 3627	Sb	728	0.030	1989-01-30	LAUC 4726	LAUC 4727	2	7.54	152.19	2
SN 1989M	Ia-norm	NGC 4579	Sb	1520	0.039	1989-06-28	LAUC 4802	LAUC 4802	4	2.49	297.42	3
SN 1990G	Ia-norm	IC 2735	Sab	10727	0.021	1990-03-19	LAUC 4982	LAUC 4984	1
SN 1990M	Ia-norm	NGC 5493	S0	2710	0.036	1990-06-15	LAUC 5033	LAUC 5034	5
SN 1990O	Ia-norm	MCG +03-44-3	Sa	9192	0.095	1990-06-22	LAUC 5039	LAUC 5039	2	12.54	54.50	2
SN 1990R	Ia-norm	NGC 4639	Sbc	1019	0.025	1990-06-23	LAUC 5039	LAUC 5039	5	7.11	160.16	2
SN 1990R	Ia-norm	UGC 11699	Sd/Irr	4857	0.096	1990-06-26	LAUC 5054	LAUC 5054	3
SN 1990Y	Ia-norm	FCCB 1147	E	11702	0.008	1990-08-22	LAUC 5080	LAUC 5083	1	16.78	...	2
SN 1991B	Ia-norm	NGC 5426	Sc	2572	0.028	1991-01-11	LAUC 5163	LAUC 5164	3
SN 1991K	Ia-norm	NGC 2851	S0	5096	0.059	1991-02-20	LAUC 5196	Matheson et al. (2001)	2
SN 1991M	Ia-norm	IC 1151	Sc	2170	0.036	1991-03-12	LAUC 5207	LAUC 5207	4	18.06	152.09	2
SN 1991O	Ia-91bg	2MASX J14243792+6545294	0.012	1991-03-18	LAUC 5233	LAUC 5233	1
SN 1991S	Ia-norm	UGC 5691	Sb	16489	0.026	1991-04-10	LAUC 5238	LAUC 5245	1	31.05	...	2
SN 1991T	Ia-91T	NGC 4527	Sbc	1736	0.023	1991-04-13	LAUC 5239	LAUC 5251	2	-10.10	347.19	2
SN 1991am	Ia-norm	MCG +06-37-6	Sb	18353	0.018	1991-07-14	LAUC 5312	LAUC 5318	1
SN 1991ak	Ia-norm	NGC 5378	Sa	3043	0.013	1991-07-15	LAUC 5309	LAUC 5311	3
SN 1991at	Ia-norm	UGC 733	Sb	12306	0.068	1991-08-19	LAUC 5336	LAUC 5347	1
SN 1991as	Ia	[M91k] 224610+0754.6	0.107	1991-08-19	LAUC 5336	LAUC 5347	1
SN 1991ay	Ia-norm	2MASX J00471896+4032336	Sb	15289	0.062	1991-09-09	LAUC 5352	LAUC 5366	1
SN 1991bd	Ia-norm	UGC 2936	Sd/Irr	3813	0.449	1991-10-12	LAUC 5367	LAUC 5367	1
SN 1991bc	Ia-norm	UGC 2691	Sb	6401	0.071	1991-10-12	LAUC 5366	LAUC 5366	2
SN 1991bb	Ia-norm	UGC 2892	Sbc	7962	0.331	1991-10-13	LAUC 5365	LAUC 5365	2
SN 1991bf	Ia-norm	MCG -05-56-027	S0	9021	0.016	1991-11-13	LAUC 5389	LAUC 5404	1
SN 1991bg	Ia-91bg	NGC 4374	E	1061	0.037	1991-12-03	LAUC 5400	LAUC 5403	8	0.14	161.88	2
SN 1991bh	Ia-norm	[M91o] 024216.2+145713.4	0.102	1991-12-07	LAUC 5401	LAUC 5404	1
SN 1991bj	Ia-02cx	IC 344	Sb	5441	0.052	1991-12-30	LAUC 5420	LAUC 5420	1
SN 1992G	Ia-norm	NGC 3294	Sc	1586	0.018	1992-02-09	LAUC 5452	LAUC 5458	2	23.41	126.76	2
SN 1992M	Ia-norm	2MASX J07150996+4525556	E	15589	0.086	1992-02-25	LAUC 5473	LAUC 5473	2
SN 1992ah	Ia-norm	2MASX J17374476+1254168	0.149	1992-06-27	LAUC 5559	LAUC 5559	1
SN 1992ap	Ia-norm	UGC 10430	Sbc	8958	0.009	1992-07-29	LAUC 5573	LAUC 5601	1
SN 1993C	Ia-norm	NGC 2954	E	3819	0.037	1993-01-27	LAUC 5699	LAUC 5701	3
SN 1993Y	Ia-norm	UGC 2771	S0	5990	0.186	1993-09-18	LAUC 5870	LAUC 5870	1	28.33	...	4
SN 1993aa	Ia-91bg	APMUKS(BJ) B230046.41-063708.1	0.041	1993-09-19	LAUC 5871	LAUC 5871	1
SN 1993Z	Ia-norm	NGC 2775	Sab	1355	0.041	1993-09-23	LAUC 5870	LAUC 5870	9	28.92	232.69	4
SN 1993ab	Ia-norm	NGC 1164	Sab	4176	0.155	1993-09-24	LAUC 5871	LAUC 5877	1
SN 1993ac	Ia-norm	CGCG 307-023	E	14690	0.162	1993-10-13	LAUC 5879	LAUC 5882	2	12.68	28.66	2
SN 1993ae	Ia-norm	IC 126	Sb	5711	0.039	1993-11-07	LAUC 5888	LAUC 5888	2	18.99	68.87	2
SN 1993aj	Ia-norm	UGC 3483	Sbc	10193	0.120	1993-12-10	LAUC 5912	LAUC 5912	1
SN 1993aj	Ia-norm	2MFGC 09481	Sb	23264	0.025	1993-12-27	LAUC 5915	LAUC 5921	3
SN 1994B	Ia-norm	[P94a] 081751.35+155320.5	...	26682	0.044	1994-01-16	LAUC 5923	LAUC 5923	2
SN 1994E	Ia	SDSS J113207.01+552138.0	...	19148	0.010	1994-03-05	LAUC 5952	LAUC 5952	1
SN 1994J	...	[P94] 095815.51+544427.4	...	16788	0.013	1994-03-05	LAUC 5971	LAUC 5974	1
SN 1994D	Ia-norm	NGC 4526	S0	447	0.023	1994-03-07	LAUC 5946	LAUC 5946	20	-12.31	114.73	2
SN 1994Q	Ia-norm	CGCG 224-104	S0	8663	0.018	1994-06-02	LAUC 6001	LAUC 6001	3	9.68	69.79	2
SN 1994S	Ia-norm	NGC 4495	Sab	4551	0.017	1994-06-04	LAUC 6005	LAUC 6005	1	1.11	...	2
SN 1994T	Ia-norm	CGCG 016-058	Sa	10390	0.020	1994-06-11	LAUC 6007	LAUC 6007	1	33.09	...	5
SN 1994U	Ia-norm	NGC 4948	Sd/Irr	1124	0.056	1994-06-27	LAUC 6011	LAUC 6011	1
SN 1994X	Ia-norm	2MASX J00152051-2453337	Sb	16668	0.013	1994-08-15	LAUC 6056	LAUC 6068	1
SN 1994ab	Ia-norm	MCG -05-50-8	Sb	10373	0.102	1994-09-17	LAUC 6089	LAUC 6094	1

Table abridged; the full table is available online—see Supporting Information.

^aSee Section 5 for more information on our SNID classifications.^bHost-galaxy morphology is taken from the NASA/IPAC Extragalactic Database (NED).^cHeliocentric redshifts listed are from NED, except the redshift of the host of SN 1991ay (2MASX J00471896+4032336) comes from LAUC 5366.^dThe Milky Way (MW) reddening toward each SN as derived from the dust maps of Schlegel et al. (1998) and includes the corrections of Peek & Graves (2010).^eEpochs of first and last spectrum are relative to B -band maximum brightness in rest-frame days using the heliocentric redshift and date of maximum reference presented in the table. For SNe with photometric information and only one spectrum in our dataset, only a Phase of First Spectrum is listed.^fJulian Date of Maximum References: (1) Tsvetkov et al. (1990), (2) Ganeshalingam et al. (2010), (3) Kimeridze & Tsvetkov (1991), (4) Ho et al. (2001), (5) Hicken et al. (2009).

Table 2: SN Ia Spectral Information

SN Name	UT Date ^a	MJD ^b	Phase ^c	Inst. ^d	Wavelength Range (Å)	Res. ^e (Å)	P.A. ^f (°)	Par. ^g (°)	Air. ^h (")	Sec. ⁱ (")	Exp. (s)	Observer(s) ^j	Reducer ^k	Flux Corr. ^l
SN 1989A	1989-04-27.000	47643.000	83.80	1	3450-9000	12	2	...	1,2	1	0
SN 1989B ^m	1989-02-15.000	47572.000	7.54	2	3450-8450	7	0	1,3	1	0
SN 1989B ^m	1989-02-21.000	47578.000	13.53	2	3450-7000	7	0	1	1	0
SN 1989B	1989-04-27.000	47643.000	78.37	1	3300-9050	12	2	...	1,2	1	0
SN 1989B	1989-07-10.000	47717.000	152.19	1	3900-6226	12	3	...	1,2,3	1	0
SN 1989M	1989-07-09.000	47716.000	2.49	1	3080-10300	12	2.5	...	1,2,3	1	0
SN 1989M	1989-07-10.000	47717.000	3.48	1	3400-10200	12	3	...	1,2,3	1	0
SN 1989M	1989-12-01.000	47861.000	146.76	1	4150-9500	12	1.5	900	1,2	1	0
SN 1989M	1990-05-01.428	48012.428	297.42	1	3930-6980	12	54	54	2.31	2.5	2100	1,2	1	0
SN 1990G	1990-03-25.000	47975.000	...	1	3932-9800	12	3	...	1,2	1	0
SN 1990M	1990-04-01.000	47982.000	...	1	3932-7060	12	1.5	...	1,4	1	0
SN 1990M	1990-07-17.000	48089.000	...	1	3920-9860	12	2	...	1,2	1	0
SN 1990M	1990-07-31.255	48103.255	...	1	3900-9900	12	48	50	4.19	1.25	1200	1,2	1	0
SN 1990M	1990-08-29.171	48132.171	...	1	3940-9850	12	229	49	3.85	1.25	1300	1,2	1	0
SN 1990M	1990-08-30.000	48133.000	...	1	6720-9850	12	229	49	4.02	2.25	1300	1,2	1	0
SN 1990O	1990-07-17.000	48089.000	12.54	1	3920-7080	12	2	...	1,2	1	0
SN 1990O	1990-07-31.396	48103.396	26.50	1	3900-7020	12	55	56	2.67	1.25	1800	1,2	1	0
SN 1990O	1990-08-29.252	48132.252	54.50	1	3900-7020	12	235	54	1.52	1.25	1400	1,2	1	0
SN 1990N	1990-07-17.000	48089.000	7.11	1	3920-9872	12	2	...	1,2	1	0
SN 1990N	1990-07-31.193	48103.193	21.25	1	3900-9900	12	55	55	2.30	1.25	900	1,2	1	0
SN 1990N	1990-08-29.153	48132.153	50.11	1	3940-9850	12	234	54	3.80	1.25	500	1,2	1	0
SN 1990N	1990-08-30.000	48133.000	50.96	1	6720-9850	12	234	54	4.23	2.25	950	1,2	1	0
SN 1990N	1990-12-17.577	48242.577	160.16	1	3900-7000	12	151	331	1.14	2.5	900	1,2	1	0
SN 1990R	1990-07-17.000	48089.000	...	1	3952-7052	12	2	...	1,2	1	0
SN 1990R	1990-07-31.423	48103.423	...	1	3900-7020	12	32	37	1.19	1.25	1200	1,2	1	0
SN 1990R	1990-08-29.279	48132.279	...	1	3900-7020	12	180	6	1.10	1.25	2400	1,2	1	0
SN 1990Y	1990-08-30.510	48133.510	16.78	1	3940-7050	12	171	351	3.07	2.25	1200	1,2	1	0

Table abridged; the full table is available online—see Supporting Information.

^aIf not rounded to the whole day, UT date at the midpoint of the observation.

^bModified JD (if not rounded to the whole day, modified JD at the midpoint of the observation).

^cPhases of spectra are in rest-frame days using the heliocentric redshift and photometry reference presented in Table 1.

^dInstruments: (1) UV Schmidt (Shane 3 m), (2) Stover Spectrograph (Nickel 1 m).

^eFWHM spectral resolution as measured from narrow sky emission lines. If we were unable to accurately measure the sky lines, the average resolution for that instrumental setup is displayed (see Section 2 for more information regarding our instrumental setups and their average resolutions).

^fObserved position angle during observation.

^gAverage parallactic angle (Filippenko 1982) during the observation.

^hAirmass at midpoint of exposure.

ⁱApproximate atmospheric seeing as measured from the FWHM of the trace of the SN. If we were unable to accurately measure the FWHM of the trace, an estimate by the observers of the average seeing from that night is displayed with only one or two significant figures.

^jObservers: (1) Alex Filippenko, (2) Joe Shields, (3) Michael Richmond, (4) Charles Steidel.

^kReducers: (1) Tom Matheson.

^lFlux Correction: (0) No correction. Negative values indicate that > 5% of the corrected flux is negative.

^mObservation has unreliable spectrophotometry due to events external to normal telescope operation and data reduction. See Section 3.2 for more information.

2 OBSERVATIONS

Over the past two decades, our group has had access to several different telescopes and spectrographs for the purpose of observing SNe. The main facility for this study was the Shane 3 m telescope at Lick Observatory. During this period, the Shane telescope has had two low-resolution spectrographs: the UV Schmidt spectrograph until early 1992 (Miller & Stone 1987) and the Kast double spectrograph since then (Miller & Stone 1993). Using these instruments we obtained 4.9 per cent and 72.3 per cent of our spectra, respectively. We also obtained a handful of spectra using the Stover spectrograph mounted on the Nickel 1 m telescope also at Lick.

We have supplemented our Lick Observatory sample with spectra obtained at the Keck Observatory. When conditions were not acceptable for our faint, primary targets (typically in twilight, or during times of bad seeing or cloudy weather), we would use one of the 10 m Keck telescopes to obtain spectra of our relatively bright (typically $R < 18$ mag), nearby SN targets. We also obtained many late-time spectra with the Keck telescopes. 16.8 per cent of our spectra were obtained using the Low Resolution Imaging Spectrometer (LRIS; Oke et al. 1995, both before and after the addition of the blue arm), 3.0 per cent were obtained using the DEep Imaging Multi-Object Spectrograph (DEIMOS; Faber et al. 2003), and 1.8 per cent were obtained using the Echelle Spectrograph and Imager (ESI; Sheinin et al. 2002).

All of these telescopes were classically scheduled. We would typically have 1 night every two weeks on the Shane telescope (near first and last quarter moon) throughout the year and 4–10 nights per year with the Keck telescopes (typically 1–2 nights near new moon in a given lunation). Recently, we have been allotted a third night per lunar cycle on the Shane telescope near new moon. Taking into account weather and instrument problems, our coverage of any given object is typically about one spectrum every two weeks. The telescope scheduling and observing method are very different from those of Matheson et al. (2008) and (Blondin et al. 2012), who observed fewer SNe Ia but with a higher cadence for each object (see Section 6.1 for further comparisons of the two spectral datasets).

All observations of our scheduled time were performed by members of the BSNIP group and PI Filippenko was present for 254 nights. Occasionally, as the result of a swap of time or for a particularly interesting object, an observer exterior to the BSNIP group would observe for our team. This sometimes resulted in slight variations in instrument configurations (such as a smaller wavelength range, for example). As mentioned above, the bulk of our data were obtained at the Lick and Keck Observatories where our average seeing was slightly greater than $2''$ and slightly greater than $1''$, respectively.

2.1 Individual Instruments

2.1.1 UV Schmidt on the Shane 3 m

The UV Schmidt spectrograph contained a Texas Instruments 800×300 pixel charge-coupled device (CCD) and our setup used a slit that was 2–3'' wide. The average resolution of our spectra from this instrument was $\sim 12 \text{ \AA}$.

2.1.2 Kast on the Shane 3 m

Until September 2008, the Kast double spectrograph used two Reticon 1200×400 pixel CCDs with $27 \mu\text{m}$ pixels and a spatial scale of $0.78'' \text{ pixel}^{-1}$, with one CCD in each of the red and blue arms of the spectrograph. Currently, the blue arm of Kast uses a Fairchild 2048×2048 pixel device with $15 \mu\text{m}$ pixels, which corresponds to $0.43'' \text{ pixel}^{-1}$. For our typical setup, we would observe with a 300/7500 grating for the red side, a 600/4310 grism for the blue side, and a D55 dichroic. This results in a wavelength range of 3300–10,400 \AA with overlap between the two arms of 5200–5500 \AA . With our typical slit of $2''$, we achieve a resolution of $\sim 11 \text{ \AA}$ and $\sim 6 \text{ \AA}$ on the red and blue sides, respectively.

2.1.3 Stover on the Nickel 1 m

The Stover spectrograph contains a Reticon 400×1200 pixel CCD and $27 \mu\text{m}$ pixels with a spatial scale of $2'' \text{ pixel}^{-1}$. Our setup used a $2.9''$ wide slit with the 600/4820 grism. This yielded an average resolution of $\sim 7 \text{ \AA}$.

2.1.4 LRIS on the Keck 10 m

When most of our dataset was obtained, LRIS used a Tektronix 2048×2048 pixel CCD with $21 \mu\text{m}$ pixels and a spatial scale of $0.211'' \text{ pixel}^{-1}$ for the red arm and two 2048×4096 pixel Marconi E2V CCDs with $15 \mu\text{m}$ pixels and a spatial scale of $0.135'' \text{ pixel}^{-1}$ for the blue arm. LRIS operated with only the red arm until 2000. The original blue-side CCD, used from 2000 to 2002, was an engineering-grade SITe 2048×2048 pixel CCD. Our typical setup would use the 400/8500 grating for the red side, either the 400/3400 or 600/4000 grism for the blue side, and the D56 dichroic, resulting in a wavelength range of 3050–9200 \AA and 3200–9200 \AA for the respective grisms. There was typically an overlap region of 5400–5800 \AA and 5400–5700 \AA for the 400/3400 and 600/4000 grisms, respectively. With our typical $1''$ slit, this setup yields resolutions of $\sim 7 \text{ \AA}$ for the red side, and either $\sim 6.5 \text{ \AA}$ or $\sim 4.5 \text{ \AA}$ for the 400/3400 and 600/4000 grisms, respectively, for the blue side.

2.1.5 DEIMOS on the Keck 10 m

DEIMOS uses a 2×4 mosaic of 2048×4096 pixel CCDs with $15 \mu\text{m}$ pixels and a spatial scale of $0.1185'' \text{ pixel}^{-1}$ for a total detector array of 8192×8192 pixels. Our typical setup would use the 600/7500 grating with a GG455 order-blocking filter, resulting in a wavelength range of 4500–9000 \AA . We would generally use a $1.1''$ slit which, along with our typical setup, would result in a resolution of $\sim 3 \text{ \AA}$. Occasionally we would use the 1200/7500 grating instead, yielding a wavelength range of 4800–7400 \AA and a resolution of $\sim 1.5 \text{ \AA}$. The slit was tilted slightly to provide better sky subtraction (see Section 3.1.4 for details).

2.1.6 ESI on the Keck 10 m

ESI has an MIT-LL 2048×4096 pixel CCD with $15 \mu\text{m}$ pixels and an average spatial scale of $0.154'' \text{ pixel}^{-1}$, with the red-order orders having a larger spatial scale than the blue-order orders. Our observations were typically performed in the echellette

mode with a 1'' wide slit in 2×1 binning mode (spatial \times spectral). This resulted in a resolution of 22 km s^{-1} across the entire wavelength range of 3900–11,000 Å.

2.2 Standard Observing Procedure

Unless there was a hardware malfunction, we would observe several dome flats at the beginning of each night (and occasionally at the end). We would also observe emission-line calibration lamps (“arcs”) at both the beginning of the night and often at the position of each object. Our final calibrations relied on observing standard stars throughout the night at a variety of airmasses. The goal was to obtain at least one standard star (in the case of single-beam spectrographs; both blue and red standard stars for double-beam spectrographs) at an airmass near 1.0 and at least one at an airmass comparable to or higher than the highest airmass of any SN observed during that night. The standard stars were typically from the catalogs of Oke & Gunn (1983) and Oke (1990), with the cool, metal-poor subdwarfs and hot subdwarfs calibrating the red and blue sides, respectively.

Most observations were made at the parallactic angle to reduce differential light loss (Filippenko 1982). Exceptions were usually at an airmass < 1.2 or when the slit was positioned at a specific angle to include a second object (the host-galaxy nucleus, a trace star, a second SN, etc.). In August 2007, LRIS was retrofitted with an atmospheric dispersion corrector (ADC; Phillips et al. 2006). With the ADC, differential light loss is substantially reduced regardless of position angle, even at high airmass.

3 DATA REDUCTION

All data were reduced in a similar, consistent manner by only a handful of people. Two people were responsible for reducing nearly half of the data while the work of only five people account for over 90 per cent of the spectral reductions presented here. There are slight differences for each instrument, but the general method is the same. Previous descriptions of our methods can be found in Matheson et al. (2000), Li et al. (2001), Foley et al. (2003), Foley et al. (2007), and Matheson et al. (2008), but the discussion below supersedes them.

3.1 Calibration

Despite differences between instruments, the general procedure for transforming raw, two-dimensional spectrograms into fully reduced, wavelength and flux calibrated, one-dimensional spectra is similar for all of our data. We will discuss differences in the procedure for the various instruments below. The general prescription is as follows.

(i) Correct for bias using an overscan region and trim the two-dimensional images to contain only the region with sky data. Our data do not typically show a bias pattern and do not have large dark currents. Therefore, we do not subtract bias frames, which would increase noise.

(ii) Combine and normalise flat-field exposures. We pay particular attention to masking emission lines from the flat-field lamps and absorption features from the air between

the flat-field screen/dome and the detector. The normalizing function is generally a low-order spline.

(iii) Correct pixel-to-pixel variations in our spectra using our flat-field exposures.

(iv) Extract the one-dimensional spectra. We use local background subtraction, attempting to remove as much host-galaxy contamination as possible. The spectra are typically optimally extracted using the prescription of Horne (1986).

However, prior to mid-1997, we did not use the optimal extraction for our Kast data but, rather, employed “standard” extractions (i.e., not optimally weighted). While this typically had minimal impact on the signal-to-noise ratio (S/N) achieved (most SNe observed with Kast are quite bright, thus standard and optimal extractions yield similar noise levels in the final spectrum), one possible effect this has on our spectra from this era is that they may be spectrophotometrically inaccurate at the ~ 5 per cent level. This is due to time-variable spatial focus variations that existed across the CCDs in the Kast spectrograph. By using the optimal extraction since then, we have significantly mitigated the effects of these variations in our data.

(v) Calibrate the wavelength scale. Using arc-lamp spectra, we fit the wavelength scale with a low-order polynomial and linearise the wavelength solution. We then make small shifts in the wavelength scale to match the night-sky lines of each individual spectrum to a master sky template.

(vi) Flux calibrate the spectra. We fit splines to the continua of our standard-star spectra, producing a sensitivity function that maps CCD counts to flux at each wavelength. These sensitivity functions are then applied to each individual SN spectrum.

(vii) Correct for telluric absorption. Using our standard-star spectra, we interpolate over atmospheric absorption regions, providing an estimate of the atmospheric absorption at a particular time and airmass. Then, accounting for the differences in airmass, we apply these corrections to our spectra, allowing for slight wavelength shifts between the “A” and “B” telluric absorption bands.

(viii) Remove cosmic rays (CRs) and make other minor cosmetic changes. In the remaining one-dimensional spectra there may be unphysical features due to CRs, chip gaps, or bad, uncorrected pixels. We interpolate over these features.

(ix) Combine overlapping spectra. For instruments with both a red and blue side (or multiple orders in the case of ESI) we combine the spectra, scaling one side to match the other in the wavelength region where the spectra overlap. For multiple, successive observations of the same object we combine the spectra to achieve the highest S/N in the resulting spectrum, weighting each spectrum appropriately (usually by exposure time).

Through mid-1997, we used our own VISTA and Fortran routines to complete all of the above steps. For about a year after that we used a combination of generic-purpose IRAF¹ routines and our own Fortran routines for our spec-

¹ IRAF: The Image Reduction and Analysis Facility is distributed by the National Optical Astronomy Observatory, which is operated by the Association of Universities for Research in Astronomy (AURA), Inc., under cooperative agreement with the National Science Foundation (NSF).

tral reductions. Since about mid-1998, we have performed our reductions using both generic-purpose IRAF routines and our own IDL scripts. Step 1 is achieved with either IRAF or IDL depending on the instrument. Steps 2–5 are generally performed with IRAF, while steps 6–9 are performed in IDL.

We consider the resulting spectra “fully reduced.” However, for a subsample of our spectra where we have multi-filtered host-galaxy photometry at the position of the SN and SN photometry near the time the spectrum was obtained, we can make additional corrections to obtain an accurate absolute flux scale as well as account for host-galaxy contamination (see Sections 3.2 and 3.3).

3.1.1 *Kast on the Lick 3 m*

The Kast spectrograph has large amplitude, variable fringing on the red-side CCD. We observe red-side dome flats at the position of each object and we apply these flats to each object individually. As the dome moves into place to take flats, we also obtain a red-side arc exposure. Using this arc spectrum we shift the wavelength solution derived from our afternoon arc exposures (which typically have more lines and are observed with a $0.5''$ slit, yielding higher-resolution lines) and apply those wavelength solutions to the appropriate SN observations. However, we still apply a small wavelength shift based on the night-sky lines later in the reduction process.

3.1.2 *Stover on the Nickel 1 m*

The Stover spectrograph does not have the ability to rotate the slit with respect to the sky; thus, all spectra obtained with this instrument were observed with a fixed sky position angle of 0° . When observations were at relatively large airmasses (as they were for some of the spectra presented here) this caused their continuum shape to be unreliable. The spectra in our dataset from the Stover spectrograph have been previously published (Wells et al. 1994; Li et al. 2001), and while strange spectrophotometric calibration issues when using this instrument with our setup and reduction routines have been noted by Leonard et al. (2002), Li et al. (2001) find no such problems.

3.1.3 *LRIS on the Keck 10 m*

The blue side of LRIS has two CCDs offset in the spatial direction (allowing a full spectrum to be on a single CCD). We typically position our objects on the slit so they will be centred on one CCD, ignoring the other CCD completely. However, in some observations circumstances dictated that objects be on the other CCD. Each CCD must be calibrated separately (different flat-field response functions, sensitivity functions, etc.). The LRIS flat-field lamp is not particularly hot, providing few photons at the bluest wavelengths of LRIS. We therefore mask this region in the flat-field response, leaving the bluest portions uncorrected for pixel-to-pixel variations.

When our dataset was obtained, the red-side CCD of the spectrograph had large fringes. We account for these fringes by applying dome flats obtained during the afternoon

or morning. We occasionally obtained internal flats at the position of an object, but we have found these to typically be worse for removing pixel-to-pixel variations than the nightly dome flats. However, there are rare instances where they were used instead of dome flats.

3.1.4 *DEIMOS on the Keck 10 m*

The long slit for DEIMOS is slightly tilted, producing slightly different wavelengths for a pixel in a given column. This tilts the night-sky lines, providing additional sampling of the lines. Since our typical procedure is not adaptable to tilted sky lines (our background subtraction would produce dipoles for every sky line), we implement a modified version of the DEEP2 DEIMOS pipeline (Newman et al. 2012; Cooper et al. 2012)² to rectify and background-subtract our spectra. The pipeline bias-corrects, flattens, traces the slit, and fits a two-dimensional wavelength solution to the slit by modeling the sky lines. This final step provides a wavelength for each pixel. The slit is then sky subtracted (in both dimensions) and rectified, producing a rectangular two-dimensional spectrum where each pixel in a given column has the same wavelength. From this point we resume our normal procedure, starting with extracting the spectrum (step 4). Since the spectrum has already been sky subtracted, we do not attempt any additional sky subtraction (which would only increase the noise) unless the SN is severely contaminated by its host galaxy.

3.1.5 *ESI on the Keck 10 m*

The CCD of ESI has several large defects which we mask before starting our reductions. These produce $\sim 50 \text{ \AA}$ gaps in our spectra, usually near $4500\text{--}4600 \text{ \AA}$. They can also affect our measurement of the trace, but this was rarely a problem for the low-redshift, relatively bright SNe presented in this paper. ESI observes 10 orders; we reduce each order individually and stitch the orders together at the end (step 9), using our standard-star observations to determine the scaling and overlap regions. We weight the spectra in the overlap by their variance in each pixel before combining. For ESI we do not linearise the wavelength solution, but instead rebin to a common velocity interval, thus producing pixels of different sizes in wavelength space.

3.1.6 *Other Instruments*

In addition to the aforementioned instruments, our dataset contains a few spectra which were obtained by observers exterior to the BSNIP group at observatories aside from Lick and Keck. These data come from the Low Dispersion Survey Spectrograph 3 (LDSS-3; Mulchaey & Gladders 2005) mounted on the 6.5 m Clay Magellan II telescope, the R.C. spectrograph mounted on the Kitt Peak 4 m telescope, and the Double Spectrograph mounted on the Hale 5 m telescope at Palomar Observatory (Oke & Gunn 1982).

² <http://astro.berkeley.edu/~cooper/deep/spec2d/>.

3.1.7 Additional Reduction Strategies

Occasionally our standard procedures produce nonoptimal spectra. In these cases we augment our procedures to produce higher-quality spectra.

For some spectra we perform a CR cleaning of the two-dimensional spectra before extraction (step 4). This procedure is done in IRAF and detects pixels that have significantly more counts than their surrounding pixels, replacing them with the local median. Since this procedure has the potential to remove real spectral features, it is not automatically performed on every spectrum.

We can obtain better sky subtraction on some spectra by performing a two-dimensional sky subtraction. This procedure fits each pixel in the spatial direction with a polynomial or spline function (usually constrained to the region near the SN position) and subtracts that fit from each pixel in that column. We have found, however, that local sky subtraction generally produces better results.

On rare occasions, we have multiple dithered images of a single object. With these images we can (after proper scaling) subtract one from another to remove residual fringing and sky lines. We can also shift the spectra spatially and combine the two-dimensional spectra to increase the S/N of the object. This can produce better traces.

For objects without a defined trace across the entire chip, we would create a trace function for the object either using the trace of a nearby object such as the host-galaxy nucleus or of a bright star (often an offset star) taken in the previous exposure at the same position as the SN.

3.2 Spectrophotometry

Using our standard reduction procedure outlined in Section 3.1, the *relative* spectrophotometry of our data is usually quite accurate. However, there are many ways in which the spectrophotometry may be corrupted. First, there are achromatic effects such as clouds that affect the *absolute* spectrophotometry. Absolute spectrophotometry is not necessary for many spectroscopic studies (although we will discuss absolute spectrophotometry in more detail in Section 3.2.2); accurate relative spectrophotometry, however, may be important. There are many reasons why the relative photometry of a spectrum may be incorrect, but variable atmospheric absorption, nonparallactic slit angles leading to differential light losses (Filippenko 1982), and incorrect standard-star spectrophotometry can all contribute significant errors. As shown below, after rigorous testing we find that the relative spectrophotometry of the BSNIP data is accurate to ~ 0.05 – 0.1 mag across most of the wavelengths covered by the spectra.

Occasionally, events external to the normal operations of the telescope and data reduction can result in questionable spectrophotometry. Instrument failures (e.g., a broken shutter) or environmental effects (e.g., nearby wild fires) are the most troublesome. There is no clear way to fully correct the spectrophotometry in these cases. Using our detailed records as well as those of Lick Observatory, we have identified several spectra where the spectrophotometry may be affected by these external factors and exclude them from any estimates of the fidelity of our spectrophotometry. Including spectra obtained with the Stover spectrograph, which does

not have a rotator and so nearly all spectra were not observed at the parallactic angle, we have flagged 88 spectra as having possibly troublesome spectrophotometry.

3.2.1 Relative Spectrophotometry

Two of the key attributes of the BSNIP sample are the large wavelength range and the consistent and thorough reduction procedures. The spectra in the sample likely have similar systematic (and hopefully small) uncertainties. The large wavelength range makes the spectra ideal for comparing near-ultraviolet and near-infrared features in a single spectrum, but such investigations will be limited by the accuracy of our spectrophotometry. Since most of the spectra in our sample have corresponding *BVRI* light curves (Ganeshalingam et al. 2010), we can test the spectrophotometry of a spectrum by comparing synthetic colours from the spectrum to those of the light curves at the time that the spectrum was obtained. In fact, this has previously been performed on some of the data presented herein (at a somewhat less rigorous level) by Poznanski et al. (2002).

For this test, we examine only the spectra of objects that have corresponding filtered light curves. To assure that our estimates of the SN colours from the photometry are accurate, we further limit the sample to spectra that have a light-curve point within 5 d of when the spectrum was taken.

We use the light-curve fitter “Multi-colour Light Curve Shape” (MLCS2k2, Jha et al. 2007) to model the filtered light curves, allowing us to interpolate between data points. We fit each filter individually to provide the largest degree of flexibility in each, and all of the fits are inspected to ensure that a good fit is obtained. In cases where the MLCS2k2 fit does not adequately reflect the data and the data are well sampled, we use a cubic spline with a Savitzky-Golay smoothing filter (Savitzky & Golay 1964).

We estimate the uncertainties in the model light curve by running a series of Monte Carlo simulations. For each data point, we randomly draw from a Gaussian distribution with mean given by the reported magnitude and σ by the photometric uncertainty to produce a simulated data point. Each simulated light curve is refit. This process is repeated 50 times and the scatter in the derived light curves is taken as the uncertainty in the model. This process is applied to objects with MLCS2k2 and spline fits.

To determine the synthetic photometry from the spectra, we convolve each spectrum with the Bessell filter functions (Bessell 1990). We calibrate our photometry by measuring the spectrophotometry of the standard star BD+17°4708 (Oke & Gunn 1983) and applying zero-point offsets to match the standard photometry. We then apply these offsets to the synthetic photometry derived from the SN spectra. The Bessell filter functions have approximate wavelength ranges of 3700–5500, 4800–6900, 5600–8500, and 7100–9100 Å for *B*, *V*, *R*, and *I*, respectively. Most of our spectra fully cover the *BVRI* bands.

There are several effects which may reduce the accuracy of our spectrophotometry. By far, the most important is galaxy contamination. Although our reduction process removes as much galaxy light as possible from a SN spectrum (see Section 3.1), some of our SN spectra are still contaminated by galaxy light. The measured synthetic colours from

galaxy-contaminated spectra will likely be vastly different from the SN colours even if our spectrophotometry is excellent. For spectra with multi-colour template images of the host galaxy and multi-colour light curves concurrent with the spectrum, we can correct for galaxy contamination to a large degree (see Section 3.3). However, this correction relies on excellent relative spectrophotometry.

We have selected a subsample of SNe that are relatively isolated from their host galaxy, so their spectra should have minimal galaxy contamination. These objects all have template images (taken after the SN had faded) that indicate minimal galaxy light. A sample of spectra of objects from this low-contamination sample of SNe is constructed to test the fidelity of our relative spectrophotometry. For this sample, we require that the spectra have $t < 30$ d and that the spectrum was obtained at the parallactic angle or at an airmass ≤ 1.2 . We present the synthetic and photometric colours for the low-contamination sample in Figure 1. Although the number of spectra in this sample is limited, they span a large range of colour.

We present a comparison of synthetic colours derived from our low-contamination and possibly contaminated spectra to those measured from light curves at the same epoch in Figure 2. An estimate of the uncertainty in the spectrophotometry can be made by examining the χ^2 per degree of freedom (dof) of the residual of the synthetic to photometric colours. The uncertainty in the photometric colours is measured by examining the residuals of the photometry measurements near the epoch of the spectrum relative to the model. The uncertainty in the relative spectrophotometry is the uncertainty added to each point which causes the residuals of the synthetic to photometric colours to have $\chi^2/\text{dof} = 1$. If $\chi^2/\text{dof} \leq 1$ with only photometric uncertainties, then the spectrophotometry does not have uncertainties larger than the photometry itself. We present estimates of the uncertainties in Table 3.

For the low-contamination sample, the spectrophotometry has a typical additional uncertainty of ≤ 0.07 mag across the entire spectrum (i.e., $B - I$), with no additional uncertainty required for $V - R$ and very little additional uncertainty (0.008 mag) required for $R - I$ across a large range of colours. Our entire sample is only slightly worse, with the additional uncertainty in $V - R$ being 0.055 mag.

This implies that the accuracy of the relative flux calibration for the low-contamination sample is difficult to assess since the uncertainties from the photometry are enough to account for the majority of the scatter in the synthetic colours (and the entire scatter for the wavelength region spanning from V to R). Nonetheless, we can place limits on the accuracy based on the additional uncertainty required and the standard deviation. From this, we find that the low-contamination sample is accurate to 5.2–6.9 per cent, 0.0–5.8 per cent, 0.7–4.5 per cent, and 6.0–9.0 per cent for the wavelength regions spanning B to V , V to R , R to I , and B to I , respectively. For the sample of objects corrected for galaxy contamination, the additional errors are similar to those of the low-contamination sample (5.3–6.5 per cent, 3.9–4.8 per cent, 4.9–5.1 per cent, and 4.5–9.2 per cent for the wavelength regions listed above), but lower than those for the entire sample (8.8 per cent, 5.1–6.2 per cent, 7.3–8.9 per cent, and 12.7–15.6 per cent), indicating that

the galaxy-contamination correction works well at least for broad-band colours.

Additionally, we have split our sample by various spectral attributes. The spectrophotometry does not depend significantly on airmass. It does depend significantly on S/N, but the spectrophotometry does not improve as S/N increases beyond $S/N \approx 20 \text{ pixel}^{-1}$. The additional uncertainties also depend slightly on the individual who reduced the spectra. However, this trend may be the result of observation and reduction techniques slowly improving over time.

We have also calculated the mean and standard deviations of the difference between the synthetic colours derived from our spectra and those measured from light curves for the various subsamples. All subsamples have a mean that is < 0.6 standard deviations from zero, with nearly all being < 0.3 standard deviations from zero. The means for the subsamples are also typically < 0.02 mag from zero, with no clear bias in any particular subsample. Furthermore, there are very few significant outliers in any colour, with only 2–5 per cent of the spectra (depending on the colour) $> 2\sigma$ away from zero.

In summary, our relative spectrophotometry is excellent. In particular, objects with little galaxy contamination or those where we are able to correct for galaxy contamination have extremely good relative spectrophotometry. This is achieved simply through our reduction methods and the relatively simple host-galaxy contamination correction outlined below; there is no spectral warping of any kind to achieve these results.

3.2.2 Absolute Spectrophotometry

As mentioned above, there are many achromatic effects which can affect our absolute spectrophotometry. We can correct for these effects if we have concurrent photometry. For these cases, we determined the synthetic photometry of our spectra and applied a multiplicative factor to scale the synthetic photometry to match our true photometry. This scaling is a byproduct of correcting for host-galaxy contamination, as described in Section 3.3.

3.3 Host-Galaxy Contamination

SNe generally do not exist in isolation. The vast majority occur within galaxies, sometimes close to or on top of complex regions such as spiral arms or H II regions. With photometry, one can correct for this by obtaining a template image after the SN has faded (or in some cases, before the star explodes), and subtracting the template from the image with the SN, leaving only the SN. Although this approach is also feasible with spectroscopy (obtaining a spectrum at the position of the SN after it has faded), it is not practical. Spectroscopy time is typically more valued, and reproducing the exact conditions at the time of the original SN observation is difficult. We do, however, have methods for reducing the galaxy contamination in a SN spectrum.

The first method is local background subtraction, as described in Section 3.1. Briefly, while extracting the SN spectrum, we model the underlying background by interpolating between background regions on either side of the SN. If the background is relatively smooth and monotonic between the background regions, this method works very well.

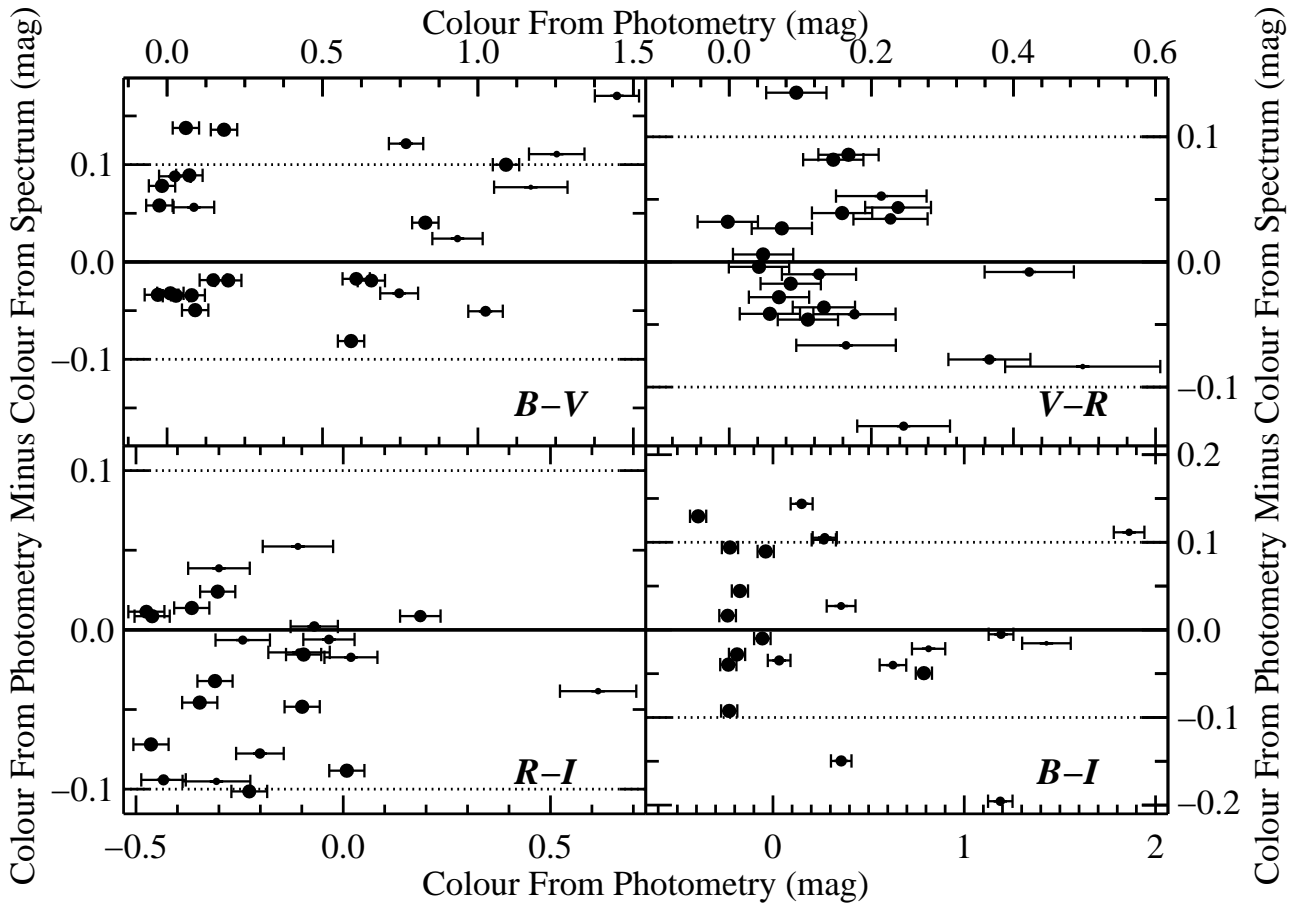


Figure 1. Comparison of synthetic colours derived from our spectra to those measured from light curves at the same epoch. Only spectra of objects where there is no obvious galaxy contamination at the position of the SN (as determined from late-time imaging) are included. Clockwise from the upper-left panel, we present the $B - V$, $V - R$, $B - I$, and $R - I$ colours. The size of each circle represents the size of the photometric uncertainty, with larger circles representing smaller uncertainty. The dotted lines in each panel are residuals of ± 0.1 mag.

However, if the SN is near the nucleus of a galaxy or on a spiral arm or other bright feature, this method can underestimate the background, leaving galaxy contamination in the SN spectrum.

We have derived a method for removing the residual galaxy contamination from our SN spectra. This approach, which we call “colour matching,” requires both SN photometry at the time the spectrum was obtained, and template colours for the host galaxy at the position of the SN. We use the host-galaxy colours to determine the spectral energy distribution (SED) of the host galaxy at the position of the SN. We then subtract the host-galaxy SED from the SN spectrum, scaled so that the synthetic photometry from the galaxy-corrected SN spectrum matches the SN photometry. This method was first presented by Foley et al. (2012); we discuss it in detail below.

3.3.1 Determining the Host-Galaxy SED

The parameter space of galaxy SEDs is well known and well behaved, allowing one to reliably reconstruct galaxy SEDs with broad-band photometry. Adopting the approach de-

scribed by Blanton et al. (2003), but updated by Blanton & Roweis (2007) to include UV wavelengths, and implemented in the IDL software package `kcorrect.v4.1.4`, we have used our $BVRI$ photometry of the host galaxy at the position of the SN and the redshifts presented in Table 1 to reconstruct the galaxy SED at the position of the SN. We perform aperture photometry on galaxy templates obtained as part of the Lick Observatory SN Search (LOSS) follow-up photometry effort (Ganeshalingam et al. 2010) using a 3 pixel ($2.4''$, similar to our Kast slit size and the typical seeing at Lick Observatory) aperture and taking the median pixel value of the image to represent the sky background. Using a 3 pixel aperture for all of our galaxy templates will represent different physical sizes depending on the distance to the galaxy. An aperture significantly different from that of the slit combined with the seeing could incorporate flux from stellar populations that do not represent the SED of the galaxy at the position of SN. As a check on how aperture size affects measured galaxy colour, we also used a 4 pixel aperture fixed at the SN position. We find excellent agreement between the colours derived using a 3 pixel aperture with a mean difference ≤ 0.02 mag. For the typical galaxy

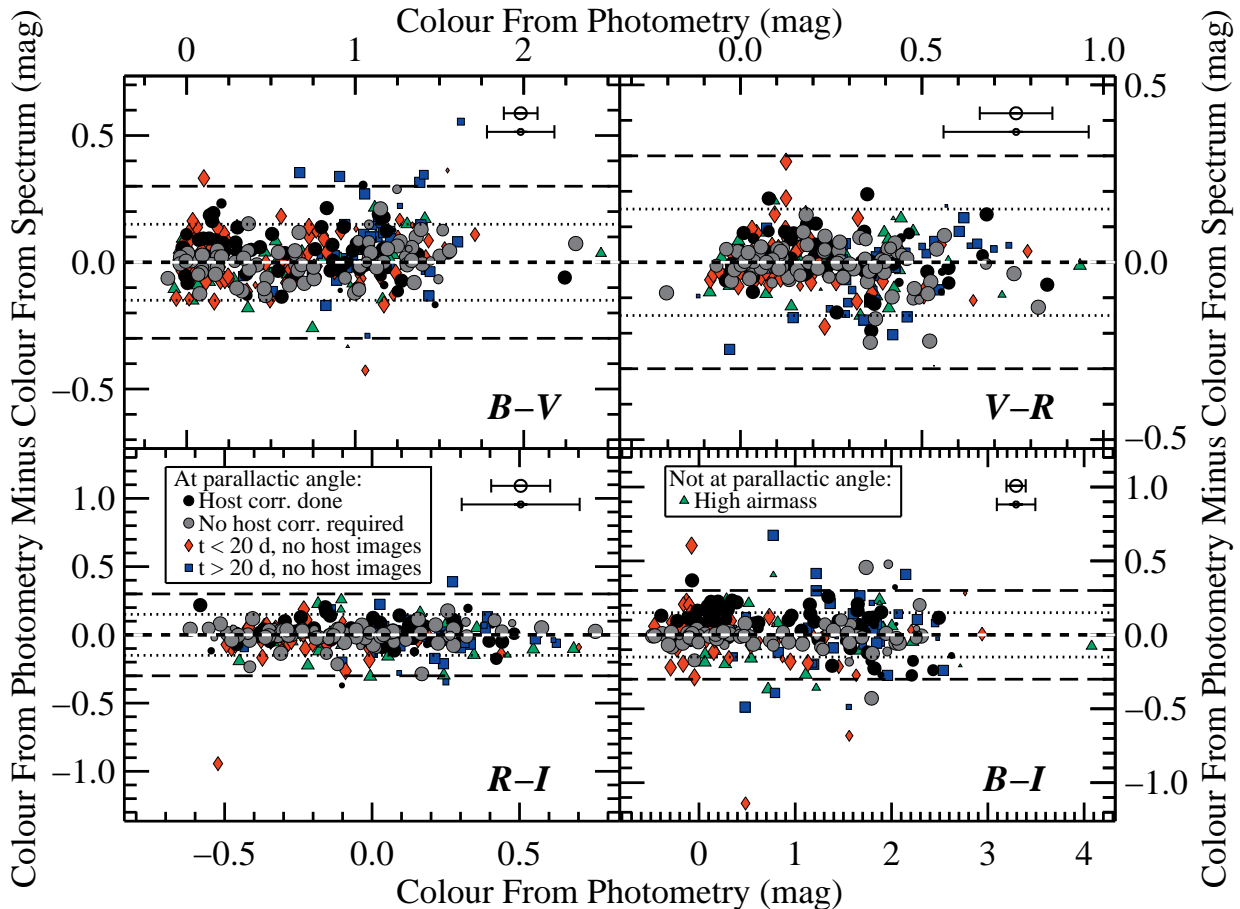


Figure 2. Comparison of synthetic colours derived from our spectra to those measured from light curves at the same epoch. Clockwise from the upper-left panel, we present the $B - V$, $V - R$, $B - I$, and $R - I$ colours. The green triangles, blue squares, red diamonds, grey circles, and black circles represent (respectively) spectra not observed at the parallactic angle and at high airmass; spectra with $t > 20$ d observed at the parallactic angle, but lacking host-galaxy images to perform host-galaxy subtraction; spectra with $t < 20$ d observed at the parallactic angle, but lacking host-galaxy images to perform host-galaxy subtraction; spectra observed at the parallactic angle, with host-galaxy images, but no host-galaxy subtraction is required; and spectra observed at the parallactic angle that have been corrected for host-galaxy contamination. The size of each symbol represents the size of the photometric uncertainty, with larger symbols representing smaller uncertainty. Representative sizes (0.1 and 0.2 mag) are shown with error bars in the upper-right corner of each panel. The dotted and long-dashed lines in each panel are residuals of ± 0.15 mag and ± 0.3 mag, respectively.

with $z < 0.5$ (which includes all redshifts presented here), the SEDs are recovered to $\lesssim 0.02$ mag in all filters (Blanton et al. 2003; Blanton & Roweis 2007).

3.3.2 Colour Matching

3.3.2.1 Motivation One approach to subtract galaxy contamination from a SN is to extract the SN without any local background subtraction, creating a spectrum that consists of all light at the position of the SN (including galaxy light) at the time of the spectrum. If one also has photometry at that epoch, one can, in principle, scale a galaxy SED to match the galaxy photometry, scale the spectrum to match the addition of the SN and galaxy photometry, and subtract the latter from the former to obtain a SN spectrum (e.g., Ellis et al. 2008). The main drawbacks of this method are that (1) one must know the proper point-spread function (PSF) of the SN and galaxy when the spectrum was obtained, and

(2) if there is a significant amount of galaxy contamination and the galaxy SED is incorrect, significant errors will be introduced.

When extracting our spectra, we attempt to remove as much galaxy contamination as possible. This approach has the benefit of reducing the galaxy contamination in the SN spectrum without introducing potential errors associated with an imprecise photometrically reconstructed galaxy SED. Also, considering the lack of precise observing information for many of our spectra (which date back over two decades), it would be difficult to estimate the correct PSF to determine the exact galaxy flux (both SED and amount) entering our slit for a given observation.

Since the galaxy colours from photometry (which are easier to measure than the absolute flux entering our slit) determine the galaxy SED, if our spectrophotometry is well calibrated then simply subtracting the galaxy SED until the

Table 3. Relative Spectrophotometric Accuracy for the BSNIP Sample

Subsample	Additional Uncertainty to Achieve $\chi^2/\text{dof} = 1$				# of Spectra (for $V - R$)
	$B - V$ (mag)	$V - R$ (mag)	$R - I$ (mag)	$B - I$ (mag)	
Low contamination	0.057	0.000	0.008	0.067	23
All spectra	0.095	0.055	0.096	0.170	306
Not parallaxic	0.089	0.048	0.107	0.158	48
Parallaxic	0.097	0.056	0.094	0.171	258
Gal. sub. – no corr.	0.088	0.053	0.073	0.140	67
Gal. sub. – corr.	0.057	0.042	0.055	0.100	81
No gal. sub.; $t > 20$ d	0.151	0.075	0.108	0.224	47
No gal. sub.; $t \leq 20$ d	0.093	0.060	0.133	0.223	63
Airmass ≤ 1.1	0.081	0.050	0.061	0.154	24
$1.1 < \text{Airmass} \leq 1.3$	0.078	0.017	0.067	0.118	37
$1.3 < \text{Airmass} \leq 1.5$	0.076	0.048	0.056	0.080	37
Airmass > 1.5	0.064	0.060	0.067	0.126	50
$S/N < 20$	0.104	0.093	0.088	0.195	18
$20 \leq S/N < 30$	0.077	0.026	0.074	0.152	16
$30 \leq S/N < 40$	0.065	0.055	0.061	0.099	27
$40 \leq S/N < 50$	0.073	0.020	0.077	0.088	31
$S/N \geq 50$	0.065	0.036	0.036	0.102	56
Reduced by T. Matheson	0.108	0.065	0.115	0.211	6
Reduced by R. Chornock	0.065	0.050	0.062	0.101	34
Reduced by R. Foley	0.058	0.041	0.040	0.107	43
Reduced by J. Silverman	0.085	0.054	0.081	0.144	51
Reduced by T. Steele	0.071	0.022	0.034	0.043	11

colours of the spectrum match those of the SN photometry will result in a SN-only spectrum.

We can demonstrate this mathematically. In general, an observed SN spectrum is defined by

$$f_{\text{spec}} = A(f_{\text{SN}} + Bf_{\text{gal}}), \quad (1)$$

where f_{spec} , f_{SN} , and f_{gal} are the vectors of fluxes in the observed spectrum, SN-only spectrum, and galaxy spectrum, respectively, and A and B are normalisation factors. One can think of A as normalizing the spectrum in an absolute sense to account for slit losses, clouds, and other achromatic effects. The parameter B controls the amount of galaxy contamination, where $B = 0$ if there is no galaxy contamination and we impose $B \geq 0$. In principle, B could be negative in order to correct for oversubtraction of galaxy light, but our testing indicates that allowing B to have negative values produces too much overfitting of the spectra.

From our image templates, we have p_{gal} , the broad-band photometry (in flux units) for the host galaxy at the position of the SN. Using MLCS2k2 (Jha et al. 2007) template light curves or spline interpolations (see Section 3.2.1), we are able to interpolate our SN photometry (independently in each band) to determine p_{SN} , the broad-band photometry (in flux units) for the SN at the time the spectrum was obtained.

We can define the function which translates spectra to synthetic broad-band photometry as P , where $P(f_{\text{SN}}) = p_{\text{SN}}$ and $P(f_{\text{gal}}) = p_{\text{gal}}$. This function is equivalent to convolving a spectrum with a filter function. Note that we impose the first relationship, while the second relationship is required by our method of determining f_{gal} .

From our spectrum, we are able to determine $p_{\text{spec}} =$

$P(f_{\text{spec}})$, the broad-band synthetic photometry (in flux units) of the spectrum, which includes both SN and galaxy light. These vectors then obey the equation

$$P(f_{\text{spec}}) = A(p_{\text{SN}} + Bp_{\text{gal}}). \quad (2)$$

For Equation 2 to be valid, we make two assumptions. The first assumption, which is already noted above, is that our spectra have accurate relative spectrophotometry. The second assumption is that B , the relative fraction of the galaxy and SN light, does not vary strongly with wavelength. From Section 3.2.1, we have shown that the relative spectrophotometry of our spectra is accurate to ~ 0.05 – 0.1 mag across large wavelength regions, comparable to the uncertainties of our photometry (after interpolating to a given date).

Solving for f_{SN} in Equation 1, we have

$$f_{\text{SN}} = A^{-1}f_{\text{spec}} - Bf_{\text{gal}}. \quad (3)$$

With a spectrum spanning at least two bands also covered by SN and galaxy photometry, one can solve for A and B from Equation 2. With galaxy photometry, the galaxy SED (f_{gal}) can be properly reconstructed. It is then simple to determine the uncontaminated SN spectrum (f_{SN}) from the galaxy-contaminated, observed spectrum (f_{spec}). We note that if $B = 0$, then Equation 3 simplifies to merely scaling the spectrum to match the photometry in an absolute sense.

3.3.2.2 Testing To test this method, we have performed Monte Carlo simulations on six different spectra with increasing galaxy contamination and appropriate photometric errors. Three of the spectra are linear (in f_{λ}) and have negative, zero, and positive slopes (corresponding to blue, flat,

and red spectra). The other three spectra are SN 2005cf at maximum brightness, ~ 1 month after maximum, and ~ 1 yr after maximum. To each of these spectra we added 5 galaxy templates, those used by the Sloan Digital Sky Survey (SDSS) to perform redshift cross-correlations, spanning early to late galaxy types.³ We measured the synthetic photometry of the spectra and galaxy templates, and for each iteration we varied the photometric data randomly using a normal distribution with width corresponding to the median error in each band for SNe and galaxies, respectively. We then performed the colour-matching technique for the galaxy-contaminated spectra with the Monte-Carlo-based photometry.

Our recovered SN spectra were compared to our input spectra, and the *differences* between the standard deviation of the residuals of the contaminated spectra and the recovered spectra are presented in Figure 3. We see that the residuals for the recovered spectra are significantly lower (i.e., the recovered spectra are better at reproducing the input spectra) than the contaminated spectra for galaxy contaminations < 70 per cent. The improvement does depend somewhat on the colour of the SN spectrum and the colour of the galaxy template, but the differences are relatively small. At higher levels of galaxy contamination, the gains are minimal in this metric, but examining the spectra, it is obvious that this technique yields impressive results even with very large amounts of galaxy contamination.

In Figure 4, we present our maximum-light and nebular-phase spectra of SN 2005cf with varying amounts of galaxy contamination. At 70 per cent galaxy contamination, where the residuals are not very large, we see that the overall shape of the spectra and spectral lines are well recovered. Even at 90 per cent galaxy contamination, where the contaminated spectra appear to be simply galaxy spectra, the method is able to recover the overall shape of the SN spectrum.

The recovered spectra differ most at the ends of the spectral coverage. This is due to the galaxy SED reconstruction being unconstrained beyond these wavelengths. If we extended our galaxy photometry beyond *BVRI*, this would improve. The emission lines of the reconstructed galaxy spectra generally have the incorrect strength. This is difficult to model with broad-band photometry, and these regions of the spectra should be ignored. The majority of the differences between the input and recovered spectra are the result of incorrect galaxy SED reconstruction from errors in the galaxy photometry. Improving the galaxy photometry or increasing the number of bands of galaxy photometry would improve the reconstruction of the galaxy SED. As the galaxy contamination increases, the errors in the reconstructed galaxy SED are amplified.

3.3.2.3 Implementation We have applied this technique to all SN spectra that have (1) *BVRI* photometry within 5 d of when the spectrum was taken, and (2) a wavelength range which spans at least two observed bands. Spectra which cover only a single observed band are scaled to match the photometry at the time of the spectrum.

The procedure used to subtract galaxy light from an observed spectrum is as follows. Using *kcorrect*, the galaxy

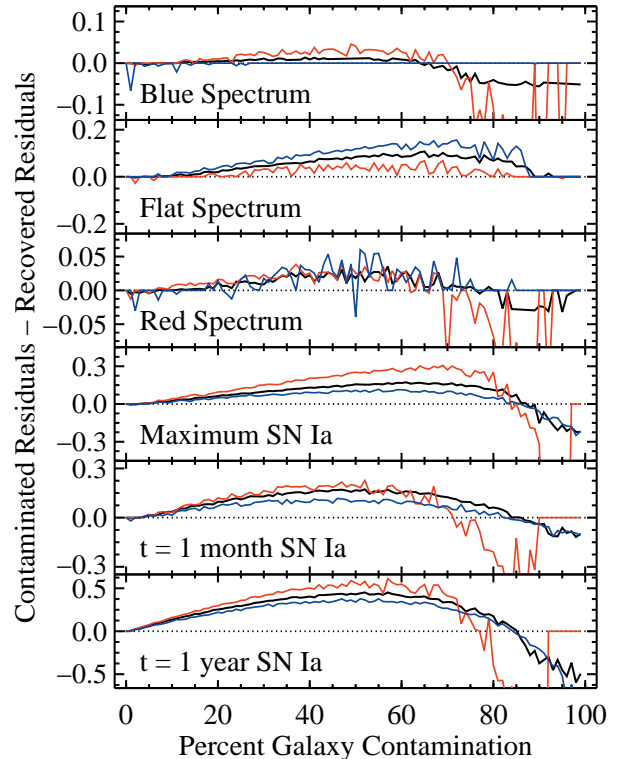


Figure 3. Differences between the median of the standard deviation of the residuals of contaminated spectra and recovered spectra after colour matching for different input spectra and galaxy templates with varying amounts of galaxy contamination. The top through bottom panels correspond to input spectra of a blue linear spectrum, a flat linear spectrum, a red linear spectrum, SN 2005cf at maximum brightness, SN 2005cf ~ 1 month after maximum, and SN 2005cf ~ 1 yr after maximum, respectively. Positive values imply that our colour-matching technique yields spectra that are closer to the input spectra than the contaminated spectra are. The horizontal dotted line in each panel represents where the residuals of the recovered spectra are equal to those of the contaminated spectra. The blue and red lines correspond to the latest and earliest galaxy templates, respectively. The black lines correspond to the average over 5 galaxy templates.

SED is reconstructed from the broad-band galaxy photometry at the position of the SN. Synthetic photometry is measured from the observed spectrum. The SN photometry at the time of the spectrum is measured from the light curves as described in Section 3.2.1. Using Equation 2 above, the factors A and B are determined using a χ^2 minimisation technique. Using Equation 3, the reconstructed galaxy SED is subtracted from the observed spectrum to produce the corrected SN spectrum.

4 DATA MANAGEMENT AND STORAGE

When preparing to present a dataset as large as ours, we required some sort of internal organised storage and retrieval method. The overall utility of our dataset will also be greatly increased by having a user-friendly interface to access the data. In addition to the final data products, all other information regarding both our photometric and spec-

³ <http://www.sdss.org/dr6/algorithms/spectemplates/>

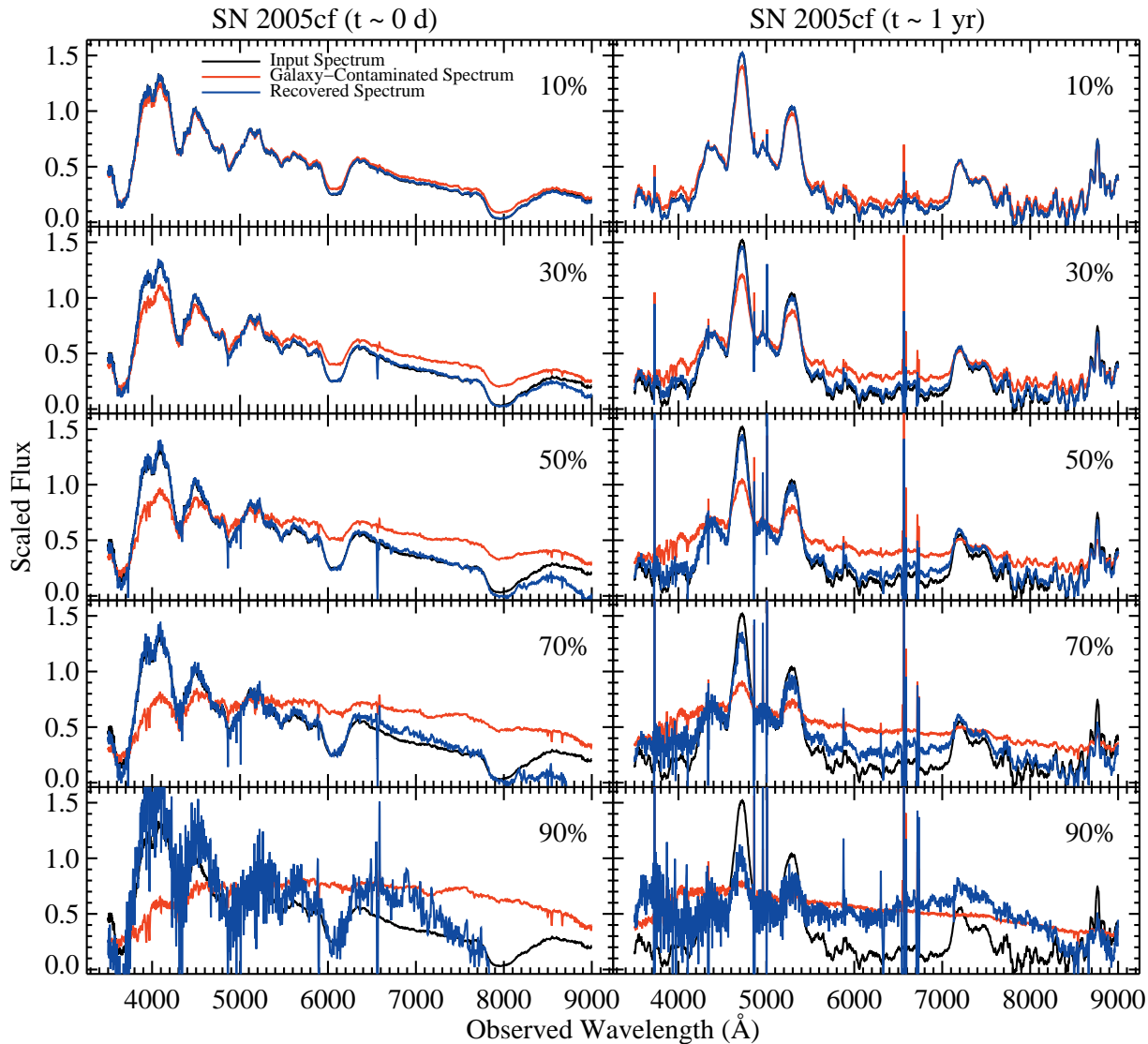


Figure 4. SN spectra used for testing the colour-matching method. The left and right columns correspond to SN 2005cf at maximum brightness and ~ 1 yr after maximum, respectively. Each row represents different amounts of galaxy contamination, from 10 per cent (*top*) to 90 per cent (*bottom*); each panel has the percent contamination labelled. Each panel shows the input spectra (black), average galaxy-contaminated spectra (from several Monte Carlo realisations, red), and average recovered spectra (from several Monte Carlo realisations, blue). The maximum-light and nebular-phase spectra have been contaminated with early-type and late-type galaxy templates, respectively. The spectra are scaled to have the same median value. Comparing the black (input) spectra to the blue (recovered) spectra gives an indication of how well the colour-matching method works. In the top panels, it is difficult to see the input spectra because of how closely the recovered spectra match the input spectra. However, even at low levels of contamination, residuals from narrow emission lines in the galaxy spectra are seen in the recovered SN spectra.

troscopic samples is stored in our SN Database (SNDB). The SNDB holds information about individual SNe (such as host-galaxy information, type, discovery information, etc.), much of which comes from external, online resources.⁴ The

⁴ For example, IAU Central Bureau for Astronomical Telegrams (<http://www.cbat.eps.harvard.edu/lists/Supernovae.html>), NASA/IPAC Extragalactic Database (NED, <http://nedwww.ipac.caltech.edu/>), and Rochester Academy of Sciences Bright Supernova List (<http://www.rochesterastronomy.org/snimages/>).

SNDB also contains information regarding individual spectra (such as observing conditions, instrument, resolution, etc.), and individual light curves (number of points, photometric accuracy, derived light-curve parameters from various fitting routines, etc.). A complete list of all fields stored in the SNDB can be found in Table 4.

The SNDB contains our entire previously published spectral dataset (both SNe Ia and core-collapse SNe) as well as all of the data presented here. It also contains photometry and light-curve information which has been previously

Table 4. SN Database (SNDB) Fields

SN Name	SNID-Determined Subtype ^a	Host-Galaxy Name
Right Ascension	Discovery Date	Host-Galaxy Type
Declination	Discoverer	Host-Galaxy Redshift (and error)
Type	Discovery Reference	SN Redshift (and error)
Type Reference	Galactic Reddening	Other Notes
Photometry and Light-Curve Information		
# of Total Photometry Points	$\Delta m_{15}(B)$ (and error)	Julian Date of B -band Maximum (and error)
# of B -band Photometry Points	Maximum B -band Magnitude (and error)	Plots of MLCS2k2 Fits ^b
# of V -band Photometry Points	$(B - V)_{B_{\max}}$ (and error)	MLCS2k2 Distance Modulus (and error) ^b
# of R -band Photometry Points	SALT/2 Distance Modulus (and error) ^c	MLCS2k2 A_V (and error) ^b
# of I -band Photometry Points	SALT/2 Light-Curve Stretch (and error) ^c	MLCS2k2 R_V (and error) ^b
# of Unfiltered Photometry Points	SALT/2 c (and error) ^c	MLCS2k2 Δ (and error) ^b
Photometry Data	SALT/2 m_B (and error) ^c	MLCS2k2 m_V (and error) ^b
Light Curve Reference(s)	SALT/2 χ^2/dof^c	MLCS2k2 χ^2/dof^b
Spectral Information		
# of Spectra of a Given SN	Exposure Time (s)	SNID Redshift (and error) ^a
UT Date of Spectrum	Position Angle (deg)	SNID Type and Subtype ^a
Filename	Parallactic Angle (deg)	SNID-Determined (Rest-Frame) Age (and error) ^a
Wavelength Range (\AA)	(Observer-Frame) Age	SNID r_{lap}^a
Airmass	Observer(s)	SNID Best Matching Template ^a
Seeing (arcsec)	Reducer	Spectral Reference(s)
Spectral Resolution(s) (\AA)	Instrument	Flux Standard Star(s)
S/N	Flux Correction ^d	

^aSee Section 5 for more information about SNID and its parameters.

^bSee Jha et al. (2007) for more information about MLCS2k2 and its parameters.

^cSee Guy et al. (2005) and Guy et al. (2007) for more information about SALT and SALT2 and their parameters.

^dSee Section 3.3 for more information about our flux corrections.

published, in addition to photometric data which have been compiled and refit by Ganeshalingam et al. (in prep.).

The SNDB uses the popular open-source software stack known as LAMP: the Linux operating system, the Apache web server, the MySQL relational database management system, and the PHP server-side scripting language. We have also implemented instances of the PHP helper classes `tar`⁵ and `JpGraph`⁶ as well as the JavaScript libraries `SortTable`⁷ and `overLIB`⁸ to improve the functionality and user friendliness of the SNDB; we are grateful to the authors of these packages. The database is stored on machines at UC Berkeley and multiple backups exist at other locations.

The primary way of accessing the SNDB is via the SN Database Public Home Page⁹. From here, users can download precompiled datasets and access our public search page, where they can define various input search criteria and query the SNDB. All SNe, spectra, and light curves that match the search criteria are returned as an HTML table. The returned information are also written to a \LaTeX table which

is linked from the Search Results Page. If spectra or photometry points are returned, users are given the option to download the actual data or plot the spectra or photometry directly in their web browser. If MLCS2k2 light-curve fits are returned, users are given the option to download a file containing the fits and probability distributions for each of the light-curve parameters.

As PI Filippenko's group at UC Berkeley publishes more spectral and photometric data of SNe of all types in the future, the SNDB will continually be updated with these newly released data. We hope that the SNDB and its free, online access will quickly become an invaluable tool to the SN community for the foreseeable future.

5 CLASSIFICATION

Optical spectra are often used to classify SNe (e.g., Filippenko 1997; Turatto 2003) into four basic types. SN II spectra are identified by strong hydrogen lines which are absent in SN I spectra. SN Ia spectra are characterised by the presence of a strong Si II $\lambda 6355$ line typically observed in absorption near 6150 \AA . SN Ib spectra lack this Si II feature but do contain strong helium lines, and finally SN Ic spectra lack strong helium lines and have a Si II $\lambda 6355$ line that is significantly weaker than those found in SNe Ia. We performed automated spectral classification of our full spectral

⁵ v2.2, Josh Barger (joshb@npt.com)

⁶ v1.27.1, Aditus Consulting (<http://www.aditus.nu/jpgraph/>)

⁷ v2, Stuart Langridge (<http://www.kryogenix.org/code/browser/sorttable/>)

⁸ v4.21, Erik Bosrup (<http://www.bosrup.com/web/overlib/>)

⁹ http://hercules.berkeley.edu/database/index_public.html

html

dataset¹⁰ using the SuperNova IDentification code (SNID; Blondin & Tonry 2007). Details of our classification algorithm are presented below.

5.1 SNID Spectral Templates

SNID classifies SN spectra by cross-correlating an input spectrum with a large database of observed SN spectra (known as “templates”) which have been deredshifted to the rest frame. In order to improve the accuracy of SNID classifications, we decided to create our own set of SNID spectral templates based on a combination of the default SNID templates and our own spectral dataset.

5.1.1 New SNID Subtypes

We began by downloading SNID v5.0¹¹ which includes a default set of templates consisting of nearby ($z < 0.1$) SNe of all types (Ia, Ib, Ic, II), as well as “NotSN” types, which includes galaxies, active galactic nuclei (AGNs), luminous blue variables (LBVs), and M stars (see Blondin & Tonry 2007, for the complete default SNID template set). SNID further divides each basic SN type into the following subtypes: Ia-norm, Ia-91T, Ia-91bg, Ia-csm, Ia-pec, Ib-norm, Ib-pec, Iib, Ic-norm, Ic-pec, Ic-broad, IIP, II-pec, IIn, and IIL.

“Norm” and “pec” identify spectroscopically “normal” and “peculiar” SNe of their respective types. Detailed descriptions of the other subtypes can be found in Blondin & Tonry (2007) and Foley et al. (2009b). In addition to these default subtypes, we have added two new SN Ia subtypes: Ia-99aa and Ia-02cx.

“Ia-99aa” SNe have spectra that resemble those of SN 1999aa-like objects (Li et al. 2001; Strolger et al. 2002; Garavini et al. 2004). Before maximum brightness, 99aa-like SNe contain a Si II $\lambda 6355$ absorption line that is stronger than those seen in 91T-like objects, but weaker than those of “normal” SNe Ia. 99aa-like objects also exhibit prominent Fe II and Fe III features at early epochs, similar to the 91T-like SNe. Moreover, 99aa-like SNe have strong Ca II H&K absorption, as do normal SNe Ia, but quite in contrast with 91T-like SNe which lack this feature; this is the main spectroscopic difference between 91T-like and 99aa-like objects. A comparison of early-time spectra of a 99aa-like SN, a 91T-like SN, and a “normal” SN Ia is shown in Figure 5. SN 99aa-like events were previously included in the Ia-91T subtype in the default set of SNID templates, but we feel that they *perhaps* represent a spectroscopically distinct subclass and therefore deserve their own subtype in SNID.

Similarly, “Ia-02cx” SNe have spectra that resemble those of SN 2002cx-like objects (e.g., Li et al. 2003; Jha et al. 2006; Foley et al. 2009a). These SNe were previously included in the Ia-pec subtype in the default set of SNID templates, but again, we believe that they represent their own subclass of events and should have their own subtype

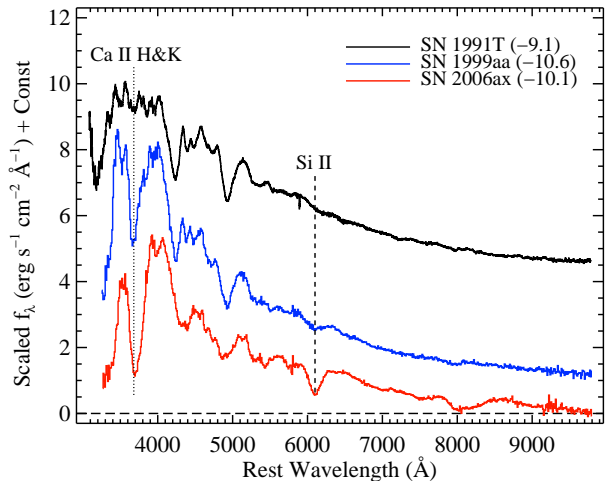


Figure 5. Spectra of SN 1991T, SN 1999aa, and the “normal” Type Ia SN 2006ax at 9.1, 10.6, and 10.1 d before maximum brightness, respectively. All spectra in the figure (as well as all spectra plotted in this work) have had their host-galaxy recession velocities removed and have been corrected for MW reddening according to the values presented in Table 1 and assuming that the extinction follows the Cardelli et al. (1989) extinction law modified by O’Donnell (1994). Notice how the Si II $\lambda 6355$ absorption feature (marked by the dashed line) increases in strength from SN 1991T to SN 1999aa to SN 2006ax. Also note the lack of Ca II H&K absorption (marked by the dotted line) in SN 1991T, which is the major difference between 91T-like and 99aa-like SNe.

in SNID. Note that for our purposes, the “Ia-pec” category refers mainly to SN 2000cx-like objects (Li et al. 2001).

We have made a few further changes to the classification scheme of SNID. Namely, Type Iib SNe (whose spectra evolve from a Type II SN to a Type Ib SN, as in SNe 1987K and 1993J; see Filippenko 1988; Filippenko et al. 1993; Matheson et al. 2000) are included *only* in the “Ib” SNID type (as opposed to being included in the “II” SNID type as well). We have also added two subtypes to the “NotSN” SNID type: quasi-stellar objects (QSOs) and carbon stars. Spectra of these objects were obtained from the SDSS Data Release 6 Spectral Cross-Correlation Templates.

5.1.2 New SNID Templates

We began constructing our new set of spectral templates for SNID by performing a literature search for the best-studied and most canonical SNe in each subtype (with emphasis on the various SN Ia subtypes). Of the objects we deemed to be “the best” examples of their respective subtypes, 30 are already included in the default set of SNID v5.0 templates (Blondin & Tonry 2007) and 30 are in our full spectral dataset, with 23 found in both sets. These objects make up version 1.0 (v1.0) of our new spectral template set. Table 5 contains information about a subset of the objects included in v1.0, as well as the rest of our final template set (the full table is available online — see the Supporting Information). We present a summary of the number of each (sub)type of SN included in the final template set in Table 6. Figure 6 shows a histogram of the ages of our SN Ia template spectra.

¹⁰ Our full dataset consists of (1) previously published SN spectra of all types, (2) SN Ia spectra which are published here for the first time, and (3) some unpublished SN spectra of non-Ia types which will be published in the future.

¹¹ <http://marwww.in2p3.fr/~blondin/software/snid/index.html>

Table 5: SNID v7.0 Spectral Templates

SN Name	Subtype	Version ^a	Age(s) ^b
SN 1988Z	IIn	1	...
SN 1989B ^c	Ia-norm	1	-6,-1,4,6,8,10,[12:14],[16:25],31,37,49,50(1)
SN 1990H	IIP	3	...
SN 1990N ^c	Ia-norm	1	-13,-6,3,5,15,18,39,50(8)
SN 1990Q	IIP	3	...
SN 1991C	IIn	2	...
SN 1991T ^d	Ia-91T	1	-12,[-10:-5],0,7,11,16,19,25,[46:47],50(5)
SN 1991ao	IIP	3	...
SN 1991av	IIn	2	...
SN 1991bg ^d	Ia-91bg	1	[0:3],[15:16],[19:20],[26:27],30,[33:34],[46:48],50(10)
SN 1992A ^c	Ia-norm	1	-5,[-1:0],[2:3],[6:7],9,12,[16:17],24,28
SN 1992H	IIP	3	...
SN 1992ad	IIP	3	...
SN 1993E	IIP	3	...
SN 1993G	IIP	3	...
SN 1993J ^d	I Ib	1	[-18:-16],-11,[-5:-2],1,[3:7],[11:13],17,20,24,[29:30],32,[35:39],41,50(38)
SN 1993W	IIP	3	...
SN 1993ad	IIP	3	...
SN 1994D ^d	Ia-norm	1	[-12:-2],0,[2:3],[10:17],19,21,24,26,28,30,40,[43:44],46,[48:49],50(9)
SN 1994I ^d	Ic-norm	1	-6,[-4:-3],[0:3],[21:24],26,30,36,38,40,50(1)
SN 1994S	Ia-norm	3	2
SN 1994W	IIn	1	...
SN 1994Y	IIn	2	...
SN 1994ae ^d	Ia-norm	1	[1:4],6,[9:11],30,36,40,50(6)
SN 1994ak	IIn	3	...
SN 1995D ^d	Ia-norm	1	4,6,8,[10:11],14,16,33,38,43,50(3)
SN 1995E	Ia-norm	3	-2
SN 1995G	IIn	2	...
SN 1995J	IIP	3	...
SN 1995V	IIP	3	...
SN 1995X	IIP	3	...
SN 1995ac ^d	Ia-91T	2	-6,24
SN 1996L ^c	IIn	1	8,34,42,50(4)
SN 1996ae	IIn	2	...
SN 1996an	IIP	3	...
SN 1996cc	IIP	3	...
SN 1997Y	Ia-norm	3	2
SN 1997ab	IIn	2	...
SN 1997br ^d	Ia-91T	2	[-9:-6],-4,[8:9],12,17,21,24,38,42,46,49,50(3)
SN 1997da	IIP	3	...
SN 1997dd	I Ib	2	...
SN 1997e ^d	Ic-broad	1	-14,[-12:-9],[-6:-4],7,[13:14],17,22,24,27,38,40,44,46,48,50(4)
SN 1997eg	IIn	2	...
SN 1998A	IIP	3	...
SN 1998E	IIn	2	...
SN 1998S ^d	IIn	1	-13,-2,[1:3],[10:11],[13:14],16,[31:32],[40:41],44,[46:47],50(37)
SN 1998bu ^d	Ia-norm	1	[-3:-1],1,[9:14],[28:44],50(9)
SN 1998bw ^c	Ic-broad	1	[8:9],[12:14],16,[18:19],21,24,[26:28],34,37,43,50(5)
SN 1998dl	IIP	3	...

Table abridged; the full table is available online—see Supporting Information.

All spectral templates are solely from our full dataset, unless otherwise noted.

^aVersion of new SNID spectral templates when object was added — 1: v1.0; 2: v2.0–v2.5; 3: v3.0–v7.0.

^bRest-frame SN age(s), rounded to nearest whole day, in days from *B*-band maximum (for SNe Ia), from *V*-band maximum (for SNe Ib/c), or from the estimated date of explosion (for SNe II). Ages of spectral templates from our dataset are calculated from the light curve references in Table 1; ages from the original SNID v5.0 set of spectral templates are from Blondin & Tonry (2007). Adjacent ages are listed in square brackets. Spectra whose age exceeds +50 days are grouped together and the number of such spectra are noted in parentheses. Many core-collapse SNe from our full spectral dataset lack age information (though we require SNe Ia templates to have age information).

^cSpectral templates are from the original SNID v5.0 set of templates only.

^dSpectral templates are from both our full dataset as well as the original SNID v5.0 set of templates.

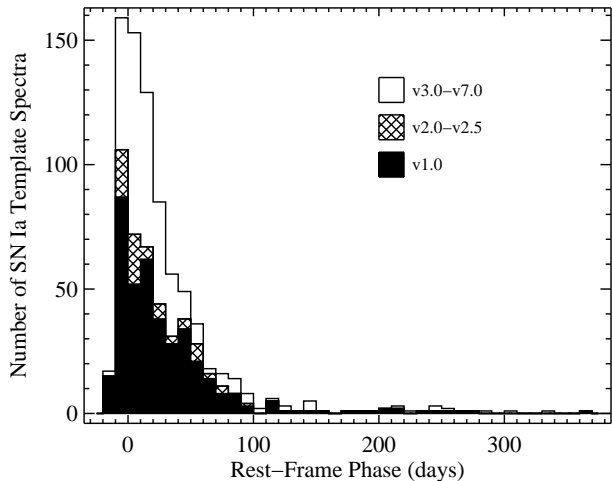


Figure 6. A histogram of the ages of our SN Ia template spectra separated by SNID template version.

For each object in v1.0, we examined only spectra that had a S/N of at least 15 pixel^{-1} , a minimum wavelength of less than 4500 \AA , and a maximum wavelength of greater than 7000 \AA . We also required that each SN Ia have a date of maximum brightness either from published sources or from Wang et al. (in prep.) so we can accurately calculate the age of each spectrum. Finally, each spectrum was visually inspected by multiple coauthors to be sure they truly represented their supposed subtype and were relatively free of host-galaxy contamination. If a spectrum passed the quantitative criteria and the by-eye inspection, it was cropped to $3500\text{--}10,000 \text{ \AA}$ (to remove edge artefacts on both ends of the spectra). If a spectrum did not cover this entire range, 50 \AA on both ends of the spectrum were removed instead. Finally, the cropped spectrum was made into a template; the result of this process was v1.0 of our new SNID templates.

To increase the number of SNe in our template set, we ran SNID (with our v1.0 templates) on our entire spectral dataset. To determine subtypes, we followed similar classification criteria to those of Blondin & Tonry (2007), requiring that the SNID r_{lap} value¹² be at least 10 and the 3 best-matching spectra from SNID all be of the same subtype. We also ignored any objects that were classified as “Ia-norm” or “IIP” since we wanted to concentrate only on relatively rare subtypes at this point and SNID is somewhat biased toward classifying objects as subtypes that have a large number of templates (such as “Ia-norm” and “IIP”). The result of this process was v2.0 of our new SNID templates. This process was repeated iteratively, running SNID with the previously created version of our spectral templates, until no more SNe passed all of the criteria. It required five additional runs to reach this convergence, resulting in v2.5 of our new SNID templates.

We continued creating a new set of spectral templates by running SNID (with our v2.5 templates) on our full spec-

tral dataset. The result of this process was v3.0 of our new SNID templates. This process was repeated iteratively, running SNID with our previously created version of the spectral templates, until no more SNe were classified and turned into templates. We finished with the creation of v7.0, our final set of new SNID templates, which we use to classify the remainder of our full spectral dataset (see Table 5 for information regarding the entire SNID template set). This v7.0 contains 1543 spectra of 277 SNe, of which 779 spectra and 134 objects are SNe Ia. Again, we show a histogram of the ages of all of our SN Ia spectral templates (separated by SNID template version) in Figure 6.

5.1.3 Final Verifications

As a sanity check, we perform final classification verifications. We ran all of our spectra of the objects in v2.5 through SNID using our v7.0 templates, and then we ran all of our spectra of the objects in v7.0 through SNID (again using our v7.0 templates). We compare the (sub)type of the best-matching template to the actual (sub)type of the object, making sure to ignore all templates of the SN currently being inspected. SNe are not used in this process if their spectra constitute > 15 per cent of all spectra in the object’s subtype.

Using only objects from v2.5 (v7.0) we find that SNID, using v7.0 of our new templates, is able to correctly classify ~ 97 per cent (~ 99 per cent) of SN Ia spectra as one of the SN Ia subtypes and non-Ia SN spectra as one of the non-Ia SN subtypes. We also find that SNID is able to correctly classify ~ 85 per cent (~ 95 per cent) of SN Ia spectra with ages ≤ 15 d past maximum brightness as the correct subtype.

We compared the classification results of our full dataset using our v7.0 templates to the results using the default set of SNID templates. The average difference between z_{gal} (the actual redshift of the host galaxy) and z_{SNID} (the redshift of the SN as determined by SNID) was found to decrease using our v7.0 templates. Furthermore, the discrepancies between t_{LC} (the spectral age derived from photometry) and t_{SNID} (the SNID-determined spectral age) improved drastically when using our v7.0 templates. Our template set also markedly suppressed the SNID-determined age bias seen near maximum brightness and $+30$ d (see Östman et al. 2011, and Section 5.3 for more on this bias). Finally, with the significant increase in the number of templates of peculiar SNe Ia and our two additional SN Ia subtypes, SNID (using our v7.0 template set) can distinguish between the various spectroscopic subtypes much better than when using the default templates. The SNID-determined subtype of ~ 15 per cent (~ 26 per cent) of the spectra (SNe Ia) presented here is different when using SNID with our v7.0 templates versus using SNID with the default templates.

5.2 Classification of Spectra

Using our v7.0 SNID templates, we can attempt to classify all of the spectra in our full dataset using criteria similar to those of Miknaitis et al. (2007) and Foley et al. (2009b). To do this we execute a series of SNID runs to separately determine the type, subtype, redshift, and age of the input spectrum. For all of the SNID runs we ignore all templates of the

¹² In SNID, the r_{lap} value is a measure of the strength of the correlation between the best-matching spectrum and the input spectrum.

Table 6. Summary of SNID v7.0 Spectral Templates

Ia (Total)	134	Ib (Total)	16	Ic (Total)	14	II (Total)	113	NotSN (Total)	29
Ia-norm	101	Ib-norm	6	Ic-norm	10	IIP	76	AGN	1
Ia-91T	3	Ib-pec	0	Ic-pec	1	II-pec	3	Gal	11
Ia-91bg	16	IIb	10	Ic-broad	3	IIIn	34	LBV	3
Ia-csm	2					IIIL	0	M-star	7
Ia-pec	1							QSO	4
Ia-99aa	7							C-star	3
Ia-02cx	4								

SN currently being inspected so that SNID will not match an object to itself, and we truncate all spectra at 10,000 Å to avoid any possible second-order light contamination. Besides these, we use the default parameters of SNID unless specifically noted below. If a spectrum was obtained within 10° of the parallactic angle (or was obtained at an airmass < 1.1) and corrected for host-galaxy contamination via our colour-matching technique (as described in Section 3.3), then we use the galaxy-subtracted spectrum in all of the SNID runs. A subset of the results of the classification algorithm presented below can be found in Table 7 (the full results are available online — see the Supporting Information).

Table 7: SNID Classification Information

SN Name	Type	Subtype	$z_{\text{SNID}}^{\text{a}}$	$t_{\text{SNID}}^{\text{b}}$	rlap	Best Match ^c					
SN 1989A	Ia	Ia-norm	0.0087 (0.0014)	83.3 (7.4)	13.1	sn99dk (Ia-norm)	0.0088 (0.0044)	71.83 (6.95)			6
SN 1989B	Ia	Ia-norm	0.0055 (0.0039)	7.5 (1.4)	17.4	sn05ki (Ia-norm)	0.0043 (0.0031)	7.96 (1.49)			14
SN 1989B	Ia	Ia-norm	0.0046 (0.0041)	23.6 (-1.0)	10.9	sn99dk (Ia-norm)	0.0042 (0.0048)	23.62 (0.68)			2
SN 1989B	Ia	Ia-norm	0.0032 (0.0015)	87.3 (13.2)	19.5	sn08ec (Ia-norm)	0.0033 (0.0027)	71.57 (9.95)			16
SN 1989B	Ia	Ia-norm	0.0029 (0.0015)	...	15.7	sn02fk (Ia-norm)	0.0035 (0.0035)	148.74 (38.33)			9
SN 1989M	Ia	Ia-norm	0.0014 (0.0053)	...	17.2	sn89B (Ia-norm)	0.0043 (0.0036)	-6.30 (5.85)			9
SN 1989M	Ia	Ia-norm	0.0022 (0.0054)	...	13.1	sn92A (Ia-norm)	0.0065 (0.0041)	6.30 (4.96)			10
SN 1989M	Ia	Ia-norm	0.0072 (0.0018)	...	10.8	sn90N (Ia-norm)	0.0059 (0.0053)	213.40 (0.00)			1
SN 1989M	Ia	Ia-norm	0.0061 (0.0000)	...	8.0	sn90N (Ia-norm)	0.0061 (0.0073)	332.50 (0.00)			1
SN 1990G	Ia	Ia-norm	0.0365 (0.0047)	9.3 (1.1)	24.2	sn98bu (Ia-norm)	0.0359 (0.0022)	9.30 (3.25)			51
SN 1990M	Ia	Ia-norm	0.0082 (0.0000)	216.9 (-1.0)	10.4	sn98bu (Ia-norm)	0.0082 (0.0057)	208.00 (6.29)			2
SN 1990M	Ia	Ia-norm	0.0077 (0.0019)	...	12.5	sn02cs (Ia-norm)	0.0091 (0.0046)	31.28 (0.00)			1
SN 1990M	Ia	...	0.0080 (0.0042)	...	12.5	sn91T (Ia-91T)	0.0101 (0.0042)	24.80 (12.41)			201
SN 1990M	Ia	...	0.0081 (0.0044)	...	13.3	sn99aa (Ia-99aa)	0.0060 (0.0042)	59.43 (21.88)			172
SN 1990M
SN 1990O	Ia	Ia-norm	0.0291 (0.0025)	15.1 (1.1)	25.6	sn07qe (Ia-norm)	0.0318 (0.0024)	16.00 (1.65)			22
SN 1990O	Ia	...	0.0287 (0.0042)	...	19.9	sn99dq (Ia-99aa)	0.0310 (0.0026)	24.09 (17.54)			275
SN 1990O	Ia	Ia-norm	0.0299 (0.0017)	55.1 (5.2)	16.1	sn02bo (Ia-norm)	0.0284 (0.0032)	56.35 (7.54)			13
SN 1990N	Ia	Ia-norm	0.0052 (0.0054)	7.1 (2.8)	22.5	sn95D (Ia-norm)	0.0030 (0.0022)	8.10 (2.93)			22
SN 1990N	Ia	Ia-norm	0.0033 (0.0019)	18.7 (3.7)	18.0	sn05cf (Ia-norm)	0.0019 (0.0032)	18.69 (3.20)			30
SN 1990N	Ia	Ia-norm	0.0031 (0.0008)	43.1 (4.3)	16.6	sn99dk (Ia-norm)	0.0021 (0.0034)	44.20 (7.14)			41
SN 1990N
SN 1990N	Ia	Ia-norm	0.0043 (0.0013)	...	19.0	sn94D (Ia-norm)	0.0043 (0.0031)	115.09 (41.77)			10
SN 1990R	Ia	Ia-norm	0.0175 (0.0010)	41.3 (1.4)	17.5	sn94D (Ia-norm)	0.0178 (0.0029)	43.20 (4.29)			34
SN 1990R	Ia	...	0.0183 (0.0042)	...	15.5	sn99aa (Ia-99aa)	0.0332 (0.0036)	26.20 (19.30)			239
SN 1990R	Ia	Ia-norm	0.0150 (0.0013)	91.1 (2.8)	18.2	sn94D (Ia-norm)	0.0172 (0.0030)	74.23 (12.81)			14
SN 1990Y	Ia	Ia-norm	0.0410 (0.0013)	16.1 (2.3)	12.7	sn02bg (Ia-norm)	0.0397 (0.0045)	-3.65 (7.14)			8
SN 1991B	Ia	Ia-norm	0.0096 (0.0021)	40.5 (-1.0)	11.3	sn05de (Ia-norm)	0.0089 (0.0045)	40.49 (3.43)			2
SN 1991B	Ia	Ia-norm	0.0098 (0.0009)	57.1 (4.2)	15.3	sn04ey (Ia-norm)	0.0097 (0.0035)	51.49 (6.27)			17
SN 1991B	Ia	...	0.0133 (0.0045)	...	14.5	sn08ds (Ia-99aa)	0.0109 (0.0033)	63.44 (28.87)			182
SN 1991K
SN 1991K	Ia	Ia-norm	0.0189 (0.0007)	91.1 (16.8)	12.0	sn07af (Ia-norm)	0.0188 (0.0043)	91.06 (15.17)			4
SN 1991M	Ia	Ia-norm	0.0055 (0.0010)	22.5 (-1.0)	10.6	sn01bg (Ia-norm)	0.0066 (0.0051)	18.91 (2.52)			2
SN 1991M	Ia	Ia-norm	0.0066 (0.0014)	...	9.1	sn05de (Ia-norm)	0.0062 (0.0056)	40.49 (7.97)			89
SN 1991M	Ia	Ia-pec	0.0096 (0.0009)	146.4 (-1.0)	14.1	sn00cx (Ia-pec)	0.0091 (0.0045)	146.31 (0.06)			2
SN 1991M	Ia	Ia-norm	0.0098 (0.0007)	...	10.1	sn90N (Ia-norm)	0.0089 (0.0054)	213.40 (0.00)			1
SN 1991O	Ia	Ia-91bg	0.0365 (0.0028)	...	12.4	sn06em (Ia-91bg)	0.0391 (0.0060)	20.95 (0.00)			1
SN 1991S	Ia	Ia-norm	0.0556 (0.0021)	38.5 (7.1)	8.7	sn94D (Ia-norm)	0.0556 (0.0051)	43.20 (11.50)			124
SN 1991T	Ia	Ia-91T	0.0029 (0.0012)	-5.6 (-1.0)	8.6	sn95ac (Ia-91T)	0.0053 (0.0057)	-5.61 (2.39)			2
SN 1991T	Ia	Ia-91T	0.0037 (0.0015)	...	14.5	sn97br (Ia-91T)	0.0042 (0.0037)	-7.40 (0.00)			1
SN 1991T	Ia	Ia-norm	0.0041 (0.0015)	...	16.2	sn94ae (Ia-norm)	0.0052 (0.0037)	9.40 (0.00)			1
SN 1991T	Ia	...	0.0081 (0.0042)	...	14.8	sn98es (Ia-99aa)	0.0057 (0.0038)	78.70 (28.43)			143
SN 1991T	Ia	Ia-norm	0.0061 (0.0011)	87.3 (6.1)	14.6	sn94D (Ia-norm)	0.0070 (0.0040)	87.19 (13.58)			12
SN 1991T
SN 1991T	Ia	...	0.0082 (0.0078)	...	23.1	sn94D (Ia-norm)	0.0080 (0.0028)	115.09 (91.53)			49
SN 1991T
SN 1991T
SN 1991am	Ia	Ia-norm	0.0604 (0.0022)	16.4 (2.9)	16.6	sn89B (Ia-norm)	0.0602 (0.0030)	13.40 (3.79)			21
SN 1991ak	Ia	Ia-norm	0.0114 (0.0010)	41.5 (2.0)	15.9	sn94D (Ia-norm)	0.0115 (0.0031)	43.20 (4.26)			31
SN 1991ak	Ia	Ia-norm	0.0112 (0.0016)	57.5 (1.5)	19.3	sn02cr (Ia-norm)	0.0100 (0.0023)	57.47 (3.98)			13
SN 1991ak	Ia	...	0.0124 (0.0042)	...	20.2	sn08ds (Ia-99aa)	0.0104 (0.0023)	63.44 (26.22)			202
SN 1991at	Ia	Ia-norm	0.0429 (0.0021)	36.4 (5.1)	12.2	sn04dt (Ia-norm)	0.0416 (0.0036)	31.97 (8.38)			12
SN 1991as	Ia	...	0.0135 (0.0042)	...	17.4	sn00cx (Ia-pec)	0.0140 (0.0034)	88.93 (77.90)			78
SN 1991ay	Ia	Ia-norm	0.0487 (0.0016)	14.5 (1.4)	17.8	sn95D (Ia-norm)	0.0471 (0.0033)	16.10 (4.14)			31
SN 1991bd	Ia	Ia-norm	0.0144 (0.0044)	23.6 (-1.0)	11.6	sn99dk (Ia-norm)	0.0139 (0.0049)	23.62 (1.36)			2
SN 1991bc	Ia	Ia-norm	0.0223 (0.0026)	17.7 (2.9)	24.0	sn90N (Ia-norm)	0.0219 (0.0024)	17.70 (4.24)			33
SN 1991bc	Ia	...	0.0233 (0.0039)	...	14.9	sn91T (Ia-91T)	0.0202 (0.0035)	75.20 (22.67)			259

Table abridged; the full table is available online—see Supporting Information.

The entries in this table match one-to-one with the entries in Table 2.

^aThe redshift uncertainty is in parentheses.

^bPhases of spectra are in rest-frame days. The phase uncertainty is in parentheses. Phase uncertainties of 0 imply that only one template was a “good” match.

^cThe best matching SNID template in the form: “template SN” (subtype) z_{SNID} (error) t_{SNID} (error) $N_{\text{good_matches}}$

5.2.1 SNID Type

If the object’s redshift is known *a priori* (from the host galaxy, usually via NED), we force SNID to use this redshift; otherwise we do not use any redshift prior. For the first attempt to determine a type, the minimum *r*lap value is set to 10. A spectrum is determined to be of a given type if the fraction of “good” correlations that correspond to this type exceeds 50 per cent. In addition, we require the best-matching SN template to be of this same type. If the spectrum’s type cannot be determined using these criteria we perform another SNID run, this time using a minimum *r*lap value of 5. This resulted in 1232 of our 1298 spectra receiving a SNID type. If the type of the input spectrum is successfully determined (using either *r*lap value), an attempt is made to determine its subtype.

5.2.2 SNID Subtype

Again, we adopt the host-galaxy redshift when available and the minimum *r*lap used to determine if the subtype is the same as was used to successfully determine the type (either 5 or 10). We also force SNID to only consider templates of the previously determined SN type. A spectrum is determined to be of a given subtype if the fraction of “good” correlations that correspond to this subtype exceeds 50 per cent. In addition, we require the best-matching SN template to be of this same subtype. If the spectrum’s subtype cannot be determined using these criteria, *and* a minimum *r*lap of 10 was used, we perform another SNID run, this time using a minimum *r*lap value of 5. This resulted in 1098 of our 1298 spectra receiving a SNID subtype. Regardless of whether SNID determines a subtype, a third run is executed to determine the redshift.

5.2.3 SNID Redshift

The SNID redshift is calculated by taking the median of all “good” template redshifts and the redshift error is the standard deviation of these redshifts. If a subtype has been successfully determined, we force SNID to only use templates of that subtype; otherwise we only use templates of the previously determined type. For this SNID run no *a priori* redshift information is used. 1232 of our 1298 spectra received a SNID redshift. If a redshift is successfully determined in this run, a fourth run is executed to calculate the age of the spectrum.

5.2.4 SNID Age

The SNID age is calculated by taking the median of all “good” template ages that have an *r*lap value larger than 75 per cent of the *r*lap value of the best-matching template. The age error is the standard deviation of these ages. Only if a subtype has been successfully determined do we attempt to calculate an age. We also require that the age error be less than either 4 d or 20 per cent of the SNID-determined age (whichever is larger). For this run, we again force SNID to adopt the host-galaxy redshift when available. If no host-galaxy redshift is known, we use the previously determined SNID redshift instead. 849 of our 1298 spectra received a SNID age.

5.3 Verifying Redshifts and Ages from SNID

It has been shown previously that SNID-determined redshifts correlate extremely well with actual redshifts of SN host galaxies (e.g., Matheson et al. 2005; Foley et al. 2009b; Östman et al. 2011). The SNID-determined redshifts (using v7.0 of our templates) agree well with the host-galaxy redshifts of our data. The dispersion about the one-to-one correspondence is only ~ 0.002 for the 1184 spectra for which the redshift is known and which SNID determined were SNe Ia and calculated a redshift. This is as good as or better than what has been found previously using much smaller samples of higher-redshift SNe (Matheson et al. 2005; Foley et al. 2009b; Östman et al. 2011). However, the majority of the largest outliers appear to have SNID redshifts that are lower than the host-galaxy redshifts. The normalised median absolute deviation (i.e., a measure of the precision of our redshifts; Ilbert et al. 2006), defined as

$$\sigma \equiv 1.48 \times \text{median} \left[\frac{|z_{\text{SNID}} - z_{\text{gal}}|}{1 + z_{\text{gal}}} \right], \quad (4)$$

is 0.002.

There is only one spectrum that is a significant outlier when comparing z_{SNID} to z_{gal} . It is 360 d past maximum brightness (according to the light curve) and we only have a small number of SN Ia templates that are this old (only 3 older than 300 d). The relative lack of good matches with old SN Ia spectra, as opposed to much younger spectra at much higher redshifts, is most likely the cause of the erroneous redshift (and age) from SNID. However, aside from this extreme case, the SNID-determined redshifts are quite accurate. Only 8 per cent (3 per cent) of the objects are more than 2σ (3σ) away from the one-to-one correspondence.

The original SNID template spectra have ages which have been corrected for the $1/(1+z)$ time-dilation factor that we expect to observe in an expanding universe (e.g., Riess et al. 1997; Foley et al. 2005; Blondin et al. 2008). Thus, SNID templates should have ages in the rest frame of the SNe.¹³ We compare the SNID-determined ages of our SN Ia spectra to their actual (rest-frame) ages as derived from their light curves and redshifts as presented in Table 1; the result is shown in Figure 7. There are 595 total spectra that SNID determined were SNe Ia (and 409 with light-curve ages ≤ 30 d) which have both SNID-determined ages and light-curve ages. The dispersion about the one-to-one correspondence for the total sample is ~ 4.1 d, and the dispersion for the sample with light-curve ages ≤ 30 d is ~ 3.3 d. Foley et al. (2009b) calculated a dispersion of 1.8 d for 59 SN Ia spectra with light-curve ages between -11 and 19.4 d at moderate to high redshift ($0.100 \leq z \leq 0.807$). We have 338 spectra in this range and calculate a dispersion of ~ 2.8 d for these data. Östman et al. (2011) obtained a dispersion of 4 d for 127 SN Ia spectra with light-curve ages between -11.7 and 67.9 d at moderate redshift ($0.03 \leq z \leq 0.32$). We have 529 spectra in this range and calculate a dispersion of ~ 3.7 d for these data.

The samples used by Foley et al. (2009b) and Östman et al. (2011) were at higher redshift than our data, and the

¹³ When creating our own SNID templates, we transformed our SN ages to the rest frame (using the redshift of the SN or the host galaxy).

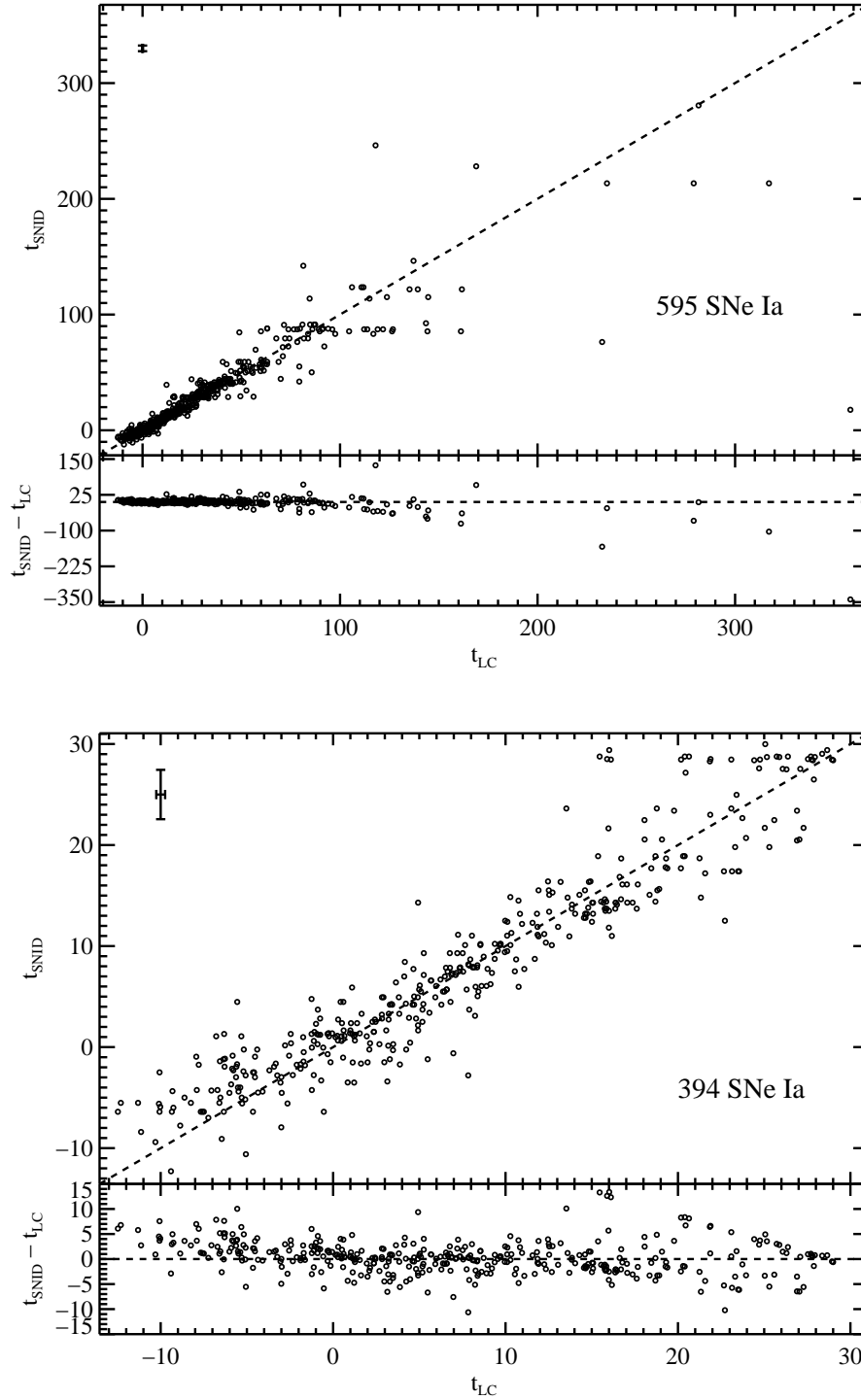


Figure 7. Comparison of rest-frame light-curve ages (t_{LC}) and SNID-determined ages (t_{SNID}) using our SNID classification scheme: all 595 spectra which SNID determined were SNe Ia and that have both SNID-determined ages and light-curve ages (*top*), and a zoom-in on the 394 SN Ia spectra with $t_{LC} \leq 50$ d and $t_{SNID} \leq 30$ d (*bottom*). The median error bar in both directions for the entire sample is shown in the top left of each plot. The bottom of both plots shows the residuals versus t_{LC} .

way in which they determined spectral ages using SNID was slightly different. Östman et al. (2011) simply used the median of all “good” template ages as the SNID-determined age. We initially attempted this relatively straightforward method for our spectra, but we soon found a significant bias in our SNID-determined ages (as compared to ages derived from the SN light curves). The bias was causing SNID-determined ages to be artificially skewed toward about +30 d for spectra which are (according to their photometry) in the range of about 23–33 d. We also observed a similar, yet weaker, version of this bias for spectra whose photometric ages were near maximum brightness as well as spectra with light-curve ages near ~ 100 d (still visible in the top panel of Fig. 7). The bias near maximum brightness is seen in the higher-redshift data presented by Östman et al. (2011), and we suggest that the bias near ages of ~ 30 d (and perhaps the one near 100 d as well) *would* have been observed in their data if their dataset had contained spectra near these epochs.

We thoroughly investigated these so-called “age attractors” and their effect on the dispersions, but unfortunately found no simple explanation for the apparent bias. In order to characterise and explain the strongest bias (near photometric ages of one month past maximum brightness), we used the default set of SNID templates, instead of our own, and again ran all of our spectra through our classification routine, only to have the bias appear even stronger than before. We examined the age and light-curve shape (as characterised by the MLCS2k2 Δ parameter; Jha et al. 2007) distributions of our v7.0 templates, the default set of SNID templates, and the light-curve ages of our entire dataset, and none of these showed any deviation at or near +30 d that might affect SNID’s age determinations. For example, Figure 6 shows a histogram of the ages of all of our SN Ia spectral templates (separated by SNID template version), and there does not appear to be any obvious bias near +30 d. Furthermore, we investigated how the strength of the bias changed with SNID-determined subtype, best-matching subtype, and r_{lap} , but saw no strong correlations.

On the other hand, all reported SNID-determined ages from Foley et al. (2009b) required that there were at least 8 good matches (and the SNID-determined age was calculated from the median age of those top 8 matches), that the age error (defined as the standard deviation of the top 8 matches) was < 6 d, and that there was a SNID-determined subtype (S. Blondin, 2011, private communication). We also attempted to use this method of SNID age determination on the BSNIP data but found that an extremely large fraction of the spectra were not being assigned a SNID age.

Various other methods of SNID age determination and verification were tested (see Table 8 for a summary), and the method that gave the best compromise between low dispersion values and large numbers of spectra being assigned a SNID age is the one that we ultimately used (described above in Section 5.2.4). Even though this new method of determining SNID ages reduces the bias near +30 d, the bias near maximum brightness (mentioned above and seen in Östman et al. 2011) is still present. It should also be noted that despite the biases that remain, over 60 per cent of our SNID-derived ages are within 1σ of the one-to-one correspondence with light-curve age.

5.4 Classification of Objects

After classifying (or attempting to classify) all of the spectra in our dataset using the method described in Section 5.2, we use the SNID information for all spectra of a given object to determine the SN’s (sub)type.

5.4.1 Classification Accuracy

To investigate the accuracy of our SN Ia classification scheme, we attempt to find correlations between the accuracy of our SN Ia subtype determination and the r_{lap} value of the best-match template, the SNID-determined age of the input spectrum, and the S/N of the input spectrum. We find that our accuracy is similarly correlated with both r_{lap} and S/N, which is unsurprising since S/N is one of the factors which determines the r_{lap} value during a SNID run. Thus, we attempt to correlate our classification accuracy with only r_{lap} and spectral age, simultaneously.

To do this, we compare the subtype we determined using our classification scheme (Section 5.2) for each SN Ia template spectrum in v7.0 to the actual subtype of the template object. If our multiple SNID runs correctly classified a given spectrum, we assigned it an “accuracy percentage” (P) of 1, and if it was misclassified it received an accuracy classification of 0. We then used the r_{lap} value of the best-matching template (r_{lap}) and the SNID-determined (rest-frame) age (t , in days) of each spectrum to fit a two-dimensional surface of the form

$$P = c_1 + c_2 \times t + c_3 \times r_{\text{lap}} \quad (5)$$

to the SNID classifications of our v7.0 SN Ia template spectra. This function was fit on a grid of phases from -20 to 200 d (in steps of 2 d) and r_{lap} values from 5 to 40 (in steps of 1). Our best-fitting values for the constants were $c_1 = 0.68 \pm 0.04$, $c_2 = -0.0014 \pm 0.0002$, and $c_3 = 0.018 \pm 0.002$, and our resulting contours are shown in Figure 8. The few spectra which are misclassified but lie above the 100 per cent contour are simply ones where even though they are misclassified, their age and r_{lap} values formally imply an “accuracy percentage” of > 100 per cent. Using our values for c_1 , c_2 , and c_3 , we can now calculate an “accuracy percentage” (P) for *any* SN Ia spectrum that has a SNID-determined age and r_{lap} (by using Equation 5).

As expected, our accuracy increases with increased r_{lap} value since r_{lap} is a measure of the strength of the correlation of the input spectrum with the best-matching SNID template. In addition, our accuracy decreases with increased age since, as noted earlier, as some subtypes of SNe Ia evolve and age their optical spectra begin to resemble those of “normal SNe Ia.”

5.4.2 Final Object Classification

For SNe with multiple spectra, we must consider each spectrum’s classification when obtaining a final classification for a given object. To do this we first determine an object’s type by counting the total number of spectra of each type for the given object. The object is then classified as the type with the highest count. If there is more than one type with the same highest count, we compare the spectra of those types only and use the type of the spectrum with the largest r_{lap}

Table 8. Number of Spectra and Dispersion of Various Methods for Determining SNID Ages

Age Range (d)	BSNIP (final) ^a		BSNIP (alternate) ^b		BSNIP (O11) ^c		BSNIP (F09) ^d		O11 ^e		F09 ^f	
	<i>N</i>	σ (d)	<i>N</i>	σ (d)	<i>N</i>	σ (d)	<i>N</i>	σ (d)	<i>N</i>	σ (d)	<i>N</i>	σ (d)
$-20 \leq t \leq 360$	595	4.1	869	5.0	860	5.4	315	3.2
$-20 \leq t \leq 30$	409	3.3	580	3.9	572	4.1	264	2.9
$-12 \leq t \leq 68$	529	3.7	757	4.5	748	4.7	314	3.2	127	4
$-11 \leq t \leq 19$	338	2.8	451	3.3	444	3.4	233	2.4	59	1.8

^aO11” = Östman et al. (2011), “F09” = Foley et al. (2009b).

^aThe method described in Section 5.2.4.

^bSimilar to the method described in Section 5.2.4. The SNID age is calculated by taking the median of all “good” template ages that have an *r*lap value larger than 75 per cent of the *r*lap value of the best-matching template. However, no other requirements are imposed.

^cThe method used by Östman et al. (2011) applied to the BSNIP data. This simply uses the median of all “good” template ages as the SNID-determined age.

^dThe method used by Foley et al. (2009b) applied to the BSNIP data. It requires that there are at least 8 good matches (and the SNID-determined age is calculated from the median age of those top 8 matches), that the age error (defined as the standard deviation of the top 8 matches) is < 6 d, and that there is a SNID-determined subtype (S. Blondin, 2011, private communication).

^eValues reported by Östman et al. (2011) using data with $0.03 \leq z \leq 0.32$.

^fValues reported by Foley et al. (2009b) using data with $0.10 \leq z \leq 0.81$.

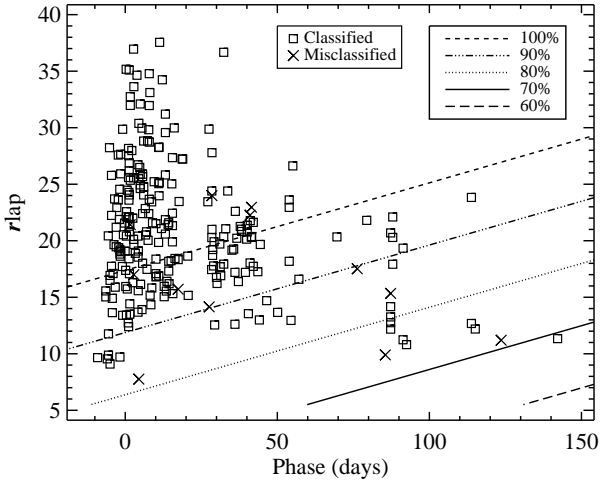


Figure 8. Accuracy of our SNID-determined SN Ia subtypes (using our classification scheme described in Section 5.2) versus SNID-determined (rest-frame) phase (in days) and *r*lap. The \square are correctly classified spectra from our v7.0 SNID templates; \times are misclassified spectra from our v7.0 SNID templates. The contours (from bottom to top) represent 60 per cent, 70 per cent, 80 per cent, 90 per cent, and 100 per cent accuracy. The few spectra which are misclassified but above the 100 per cent contour are due to the fact that we fit all v7.0 template spectra and thus a handful of misclassified objects formally have accuracies above 100 per cent.

(though we add a “?” to the type to denote our uncertainty regarding the classification).

For each object whose definite type has been determined (i.e., no trailing “?”) and that *is not* a SN Ia, we assign a subtype by counting the total number of spectra of each

subtype for the given object. The SN is then classified as the subtype with the highest count. If there is more than one subtype with the same highest count, we cannot accurately determine the subtype and thus classify the object as simply the previously determined type.

For each object that we have determined is a definite SN Ia (i.e., no trailing “?”), we calculate the “accuracy percentage” (P) for each spectrum of that object using Equation 5. We then combine the “accuracy percentages” of all of the spectra of the given SN to calculate the *maximum* probability that it is of each subtype. For example, if a spectrum has an “accuracy percentage” of P , then that is a measure of the probability that the spectrum is of subtype m (where subtype m is the subtype determined by our classification scheme in Section 5.2). This means that $1 - P$ is the probability that this spectrum is any of the other SN Ia subtypes, and it is in fact the *maximum* probability that the spectrum is of subtype n for any $n \neq m$. Therefore, we can combine the “accuracy percentages” for multiple spectra of different subtypes to calculate a maximum probability for each subtype,

$$\tilde{P}_m = \frac{\prod_{n=m} P_n \times \prod_{n \neq m} (1 - P_n)}{k_m}, \quad (6)$$

where \tilde{P}_m is the maximum probability the given object is of subtype m , the first product is over all spectra whose subtype (n) is equal to m , the second product is over all spectra whose subtype (n) is not equal to m , and k_m is a normalisation constant for subtype m defined as

$$k_m = \prod_{n=m} P_n \times \prod_{n \neq m} (1 - P_n) + \prod_{n=m} (1 - P_n) \times \prod_{n \neq m} P_n. \quad (7)$$

Once we calculate the maximum probability for each subtype, we classify the given object as the subtype with the largest such probability.

Table 9. Summary of Final SN Classifications

SNID		Adjusted	
(Sub)Type	#	(Sub)Type	#
Ia	94	Ia	37
Ia?	2	Ia?	0
Ia-norm	430	Ia-norm	459
Ia-91T	3	Ia-91T	7
Ia-91bg	25	Ia-91bg	46
Ia-csm	0	Ia-csm	1
Ia-pec	0	Ia-pec	1
Ia-99aa	2	Ia-99aa	13
Ia-02cx	7	Ia-02cx	10
Ic	1	Ic	0
Ic-norm	1	Ic-norm	0
II	1	II	0
IIP	3	IIP	0
IIn	1	IIn	0
Gal	2	Gal	0
Unknown	10	Unknown	8

SNID is merely a tool, albeit a useful one for determining spectral subtypes of SNe, but ultimately humans classify SN spectra. Thus, we visually inspected any objects in our dataset that were classified as “Ia” or “Ia?” (with no subtype) or as any of the non-SN Ia subtypes, in addition to any object that had spectra that were classified as more than one SN Ia subtype. From these visual inspections we changed a handful of the final object classifications from what our SNID-based classification algorithm would have yielded. We also forced all objects that were v7.0 SNID templates to be their actual subtype. These final (sub)type determinations can be found in Table 1; we also present a summary of the final (sub)type determinations from SNID, as well as our adjusted classifications, in Table 9.

Of all of the v7.0 template objects (which include SNe Ia as well as other SN types), 95 per cent were classified as the correct type by SNID and 86 per cent were classified as the correct subtype by SNID. We were unable to determine a type (subtype) for 2 per cent (7 per cent) of the v7.0 template objects using our aforementioned SNID-based classification scheme. Of solely the v7.0 template objects that are SNe Ia, 99 per cent received the correct type classification from SNID and 92 per cent the correct subtype classification, and we could determine a type and subtype from SNID for all of the v7.0 template SNe Ia. These are more informative and more accurate percentages than those from the simple sanity checks that were discussed in Section 5.1.3.

Of the 582 SNe Ia that are presented in this paper, our SNID-based algorithm classifies 96.8 per cent of them as SNe Ia, 1.5 per cent as other SN types, and we are unable to classify 1.7 per cent. Over half of the spectra of objects that are classified by SNID as non-Ia types or that are unclassified are relatively old and/or noisy, and thus it is not surprising that our classification scheme failed on these observations. A few spectra of these objects are heavily contaminated by host-galaxy light and lacked sufficient photometry for us to apply our galaxy-correction algorithm (Section 3.3), and so again it is reasonable that these are not correctly classified. When it was not clear from our own spectra that these

objects were SNe Ia, we relied on previous spectral classifications from the literature. In addition, some of the objects which were classified as non-Ia types are well-known, peculiar SNe Ia (including a few of our v7.0 SNID templates), but we do not have enough templates of other objects of their subtype at similar ages for SNID to get good matches to our observations. This is most likely responsible for many of SNID’s “Ia” (with no definitive subtype) and “Ia?” classifications as well, and is partially why we visually reinspected these objects.

5.4.3 Relative Fractions of Subtypes

Even though our SN Ia spectral sample is not complete by any rigorous definition and suffers from multiple observational biases, it is still illuminating to calculate the relative fractions of SN Ia subtypes (as determined by SNID) in our dataset. Of the objects for which SNID determines a SN Ia subtype, 92.1 per cent are normal, 5.4 per cent are 91bg-like, 0.6 per cent are 91T-like, 0.4 per cent are 99aa-like, and 1.5 per cent are 02cx-like. These fractions are listed in Table 10, along with those from other SN Ia studies. For the purposes of comparing these percentages to values in the literature, we will follow Li et al. (2011) and combine 99aa-like objects with 91T-like objects, yielding 1.0 per cent for this group. If, as we did when creating our new SNID templates in order to get more accurate subtype classifications, we require spectra to have ages less than 15 d past maximum brightness and $S/N > 15 \text{ pixel}^{-1}$, then we find that of these objects 90.7 per cent are normal, 6.5 per cent are 91bg-like, 1.9 per cent are 91T/99aa-like, and 0.9 per cent are 02cx-like.

In the volume-limited sample of Li et al. (2011), 70 per cent of SN Ia were normal, while 15 per cent were 91bg-like, 9 per cent were 91T/99aa-like (only a lower limit, however), and 5 per cent were 02cx-like. The slightly higher redshift ($\bar{z} = 0.17$) sample of Östman et al. (2011) detected only a few probable peculiar SNe Ia, but they calculate that 7–32 per cent of local SNe Ia should be 91T/99aa-like. The even higher redshift ($\bar{z} \approx 0.35$) sample of Foley et al. (2009b) found that 4–19 per cent were 91T/99aa-like, while they had no 91bg-like objects in their dataset.¹⁴ However, an analysis of the companion photometry to much of the spectroscopic sample presented here (Ganeshalingam et al. 2010) finds (using SNID as described in this work) that 80.6 per cent of their SNe Ia are normal, 10.9 per cent are 91bg-like, 5.5 per cent are 91T/99aa-like, 2.4 per cent are 02cx-like, and 0.6 per cent are Ia-pec (i.e., SN 2000cx, which SNID classified herein as a Ia-norm since we have no other SNID templates of 00cx-like objects). These percentages are closer to our fractions of subtypes than the complete sample presented by Li et al. (2011). This likely comes from the fact that for most of the project’s lifetime, BSNIP has had a strong focus on spectroscopically monitoring SNe Ia that were being concurrently observed photometrically as part of the sample presented by Ganeshalingam et al. (2010).

The main differences between our SNID-determined

¹⁴ Foley et al. (2009b), after correcting for various biases, expected only 1–4 91bg-like objects based on the Li et al. (2001) percentages.

Table 10. Percentages of SN Ia Subtypes

	BSNIP (Total)	BSNIP (Cut) ^a	G10	L11 ^b	O11	F09
\bar{z}	0.0283	0.0219	0.0194	0.0132	0.17	0.35
Ia-norm	92.1	90.7	80.6	70	97.9	81–96
Ia-91bg	5.4	6.5	10.9	15	0.0	0
Ia-91T/99aa	1.0 ^c	1.9 ^d	5.5	9	1.4 ^e	4–19
Ia-02cx	1.5	0.9	2.4	5	0.0	0
Ia-pec	0.0	0.0	0.6	0	0.7	0

^a“G10” = Ganeshalingam et al. (2010), “L11” = Li et al. (2011),
^b“O11” = Östman et al. (2011), “F09” = Foley et al. (2009b).
^cOnly spectra with ages less than 15 d past maximum brightness
and S/N > 15 pixel⁻¹.
^dA volume-limited sample.
^e0.6 per cent are 91T-like and 0.4 percent are 99aa-like.
^f1.0 per cent are 91T-like and 0.9 percent are 99aa-like.
^gEven though only 1.4 per cent of the sample from Östman
et al. (2011) were classified as Ia-91T/99aa, they calculate that
7–32 per cent of local SNe Ia should be 91T/99aa-like.

fractions of SN Ia subtypes and those found in the complete sample of Li et al. (2011) is that we classify too many objects as normal and not enough as 91T/99aa-like and 91bg-like. This can possibly be explained by the fact that spectra of these peculiar SNe Ia (especially 91T/99aa-like objects) resemble spectra of normal SNe Ia within a week or two after maximum brightness (introducing the so-called “age bias”; Li et al. 2001). Thus, some of our Ia-norm objects may in fact be 91T/99aa-like SNe Ia, but the spectra in our dataset were obtained at too late an epoch to distinguish between the two subtypes. Since there are many more normal SNID templates than peculiar templates, these objects will ultimately get classified as normal. Furthermore, it is possible that some objects have essentially normal spectra and are classified as Ia-norm by SNID, but have slowly (quickly) declining light curves and are thus *photometrically* classified as 91T/99aa-like (91bg-like) by Li et al. (2011). This interesting possibility will be investigated further in future BSNIP papers.

Many of the non-normal SNe Ia that we classify in our dataset have already been noted as peculiar in the literature (either in unrefereed circulars or published papers). However, there are still a few peculiar classifications that we publish here for the first time. Details regarding these interesting individual objects can be found in Section 6.2.

6 THE BSNIP SAMPLE

Our SN Ia spectral dataset consists of a total of 1298 spectra of 582 SNe Ia observed from 1989 through the end of 2008, representing nearly 470 hr of telescope time. 1159 spectra of 563 objects are published here for the first time. Plots of all of the fully reduced spectra as well as (for the objects with multi-band SN and galaxy photometry) galaxy-subtracted spectra (as discussed in Section 3.3) presented in this work are available online — see the Supporting Information. Spectral sequences for all objects in our dataset with more than

7 spectra can be found online (see the Supporting Information).

6.1 Sample Characteristics

If we remove objects where we have no light-curve information, leaving only spectra with phase (and light-curve shape) information, the sample is reduced to 914 (770) spectra of 321 (251) SNe Ia. If we further restrict ourselves to objects with relatively well-sampled, filtered light curves, retaining only those objects with precise distance measurements, our dataset contains 584 spectra of 199 SNe Ia. Finally, if we only count spectra which have reasonable estimates of multi-filtered SN magnitudes at the time of the spectrum and measurements of the host-galaxy colours at the position of the SN, providing accurate flux-calibrated, galaxy-subtracted spectra (see Section 3.3 for more information), our sample contains 234 spectra of 95 SNe Ia.

This dataset has ~ 3 times the number of spectra and ~ 18 times the number of objects as the sample of Matheson et al. (2008). Due to the scheduling of their telescope time, their dataset consisted mainly of well-sampled spectroscopic time series of a handful of SNe Ia, averaging 13.5 spectra per object. By contrast, the BSNIP sample consists of ~ 2.2 spectra per object, showing our emphasis on the total number of objects rather than the number of spectra per object. The histogram of the number of spectra per object for our sample can be seen in the top-right panel of Figure 9. Thus, our sample (emphasizing the total number of objects) and the sample of Matheson et al. (2008) (emphasizing the number of spectra per object) are complementary. Furthermore, as mentioned in Section 2, our spectra typically cover 3300–10,400 Å, compared to the typical 3700–7400 Å wavelength range of the spectra from Matheson et al. (2008).

All of the SNe Ia in our dataset have $z \leq 0.2$, and the vast majority (89.6 per cent) have $z \leq 0.05$. The distribution of redshifts for all of our SNe Ia (as well as just those with phase information) is shown in the left panels of Figure 9. The average redshift of the full sample of objects presented

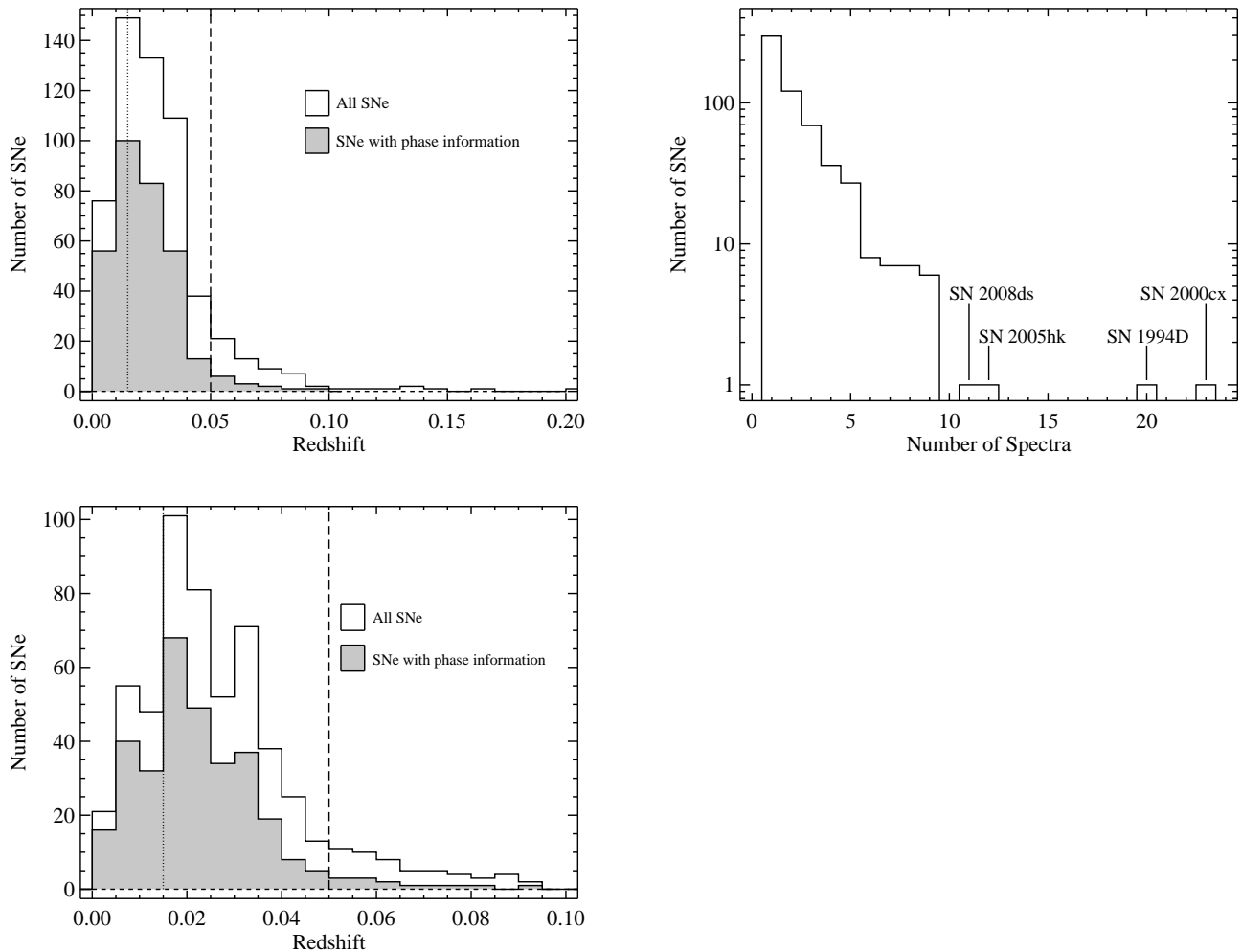


Figure 9. A histogram of the redshifts of all of the SNe Ia in our sample (*top left*) and a zoom-in on those objects with $z \leq 0.1$ (*bottom left*). The shaded regions represent objects for which we have phase information (i.e., a date of maximum brightness). The dotted vertical line ($z = 0.015$) is approximately the redshift above which peculiar velocities can be ignored in cosmological calculations (see, e.g., Astier et al. 2006). The dashed vertical line ($z = 0.05$) represents our approximate 90 per cent cutoff; i.e., ~ 90 per cent of our SNe Ia have redshifts less than 0.05. Our average redshift is about 0.0283 and our median uncertainty is 0.00004. A histogram of the number of spectra versus the number of objects in our SN Ia sample (*top right*). Our average is ~ 2.2 spectra per object.

here is about 0.0283 and the median uncertainty is 0.00004 (as determined from the redshift uncertainties reported in NED). About 78 per cent of our SNe Ia have $z \geq 0.015$ (which is approximately the redshift above which peculiar velocities can be ignored in cosmological calculations; see, e.g., Astier et al. 2006). 17 of our objects have unknown host-galaxy redshifts, but all of the spectra of these objects received a redshift from our SNID classification scheme (Section 5.2).

As mentioned above, many of our spectra have phase information from photometric observations; the distribution of phases for all of our spectra is shown in the left panels of Figure 10. We have 147 spectra of 114 SNe Ia before maximum brightness, and 245 (107) spectra of 181 (96) objects within 7 d (3 d) of maximum brightness. Our sample also contains 34 spectra of 20 SNe Ia older than 180 d past maximum brightness. The median uncertainty of our phases is 0.38 d, though the practical uncertainty is more like 0.5 d

(Ganeshalingam et al. 2010). The right panels of Figure 10 show the distribution of the phase of each SN Ia at the time of its first spectrum.

As mentioned above, many of our SNe have light-curve shape information (as characterised here by the MLCS2k2 Δ parameter; Jha et al. 2007); the distribution of Δ values for all of these objects is shown in the top-left panel of Figure 11. In the histogram we also denote each object’s final SNID classification (Section 5.4.2). The Δ values come from previously published photometric data which have all been compiled and fit by Ganeshalingam et al. (in prep.). The average Δ for our dataset is ~ 0.12 , and the median Δ and uncertainty are about -0.03 and 0.035 , respectively. Our SNe Ia span most of the standard range of Δ values (about -0.4 to 1.6 , e.g., Hicken et al. 2009).

The bottom-left panel of Figure 11 presents the host-galaxy redshift of our SNe Ia versus their Δ values. Our dataset covers most of the range of Δ values at the low-

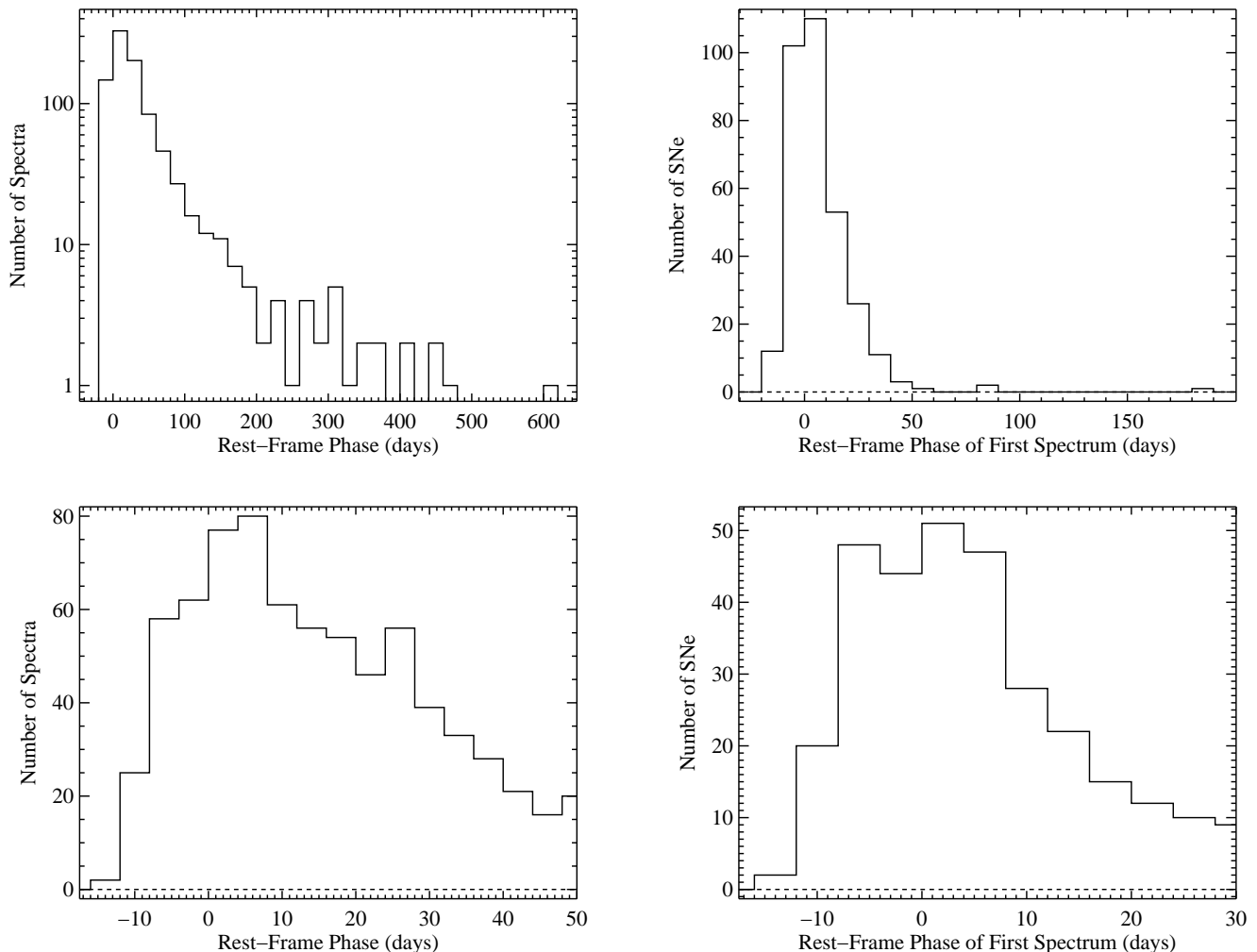


Figure 10. A histogram of the phases of all of the spectra in our sample for which we have phase information (*top left*) and a zoom-in on those spectra with $t \leq 50$ d (*bottom left*). Our median uncertainty is 0.38 d. A histogram of the phase of each SN Ia (for which we have phase information) at the time of our first spectrum (*top right*) and a zoom-in on those spectra with $t_{\text{first}} \leq 30$ d (*bottom right*). Our median uncertainty is 0.38 d.

est redshifts, but our coverage decreases at higher redshifts. SNe Ia with large Δ are the fainter, faster-evolving objects (Jha et al. 2007), and thus we have fewer of those (relative to smaller Δ objects) in our sample at higher redshifts. The right panels of Figure 11 present the phase of each spectrum versus their Δ values. Analogous to the bottom-left panel of the same figure, our sample spans most of the standard range of Δ values at early times, but the coverage begins to drop off at ~ 40 d past maximum brightness. Once again, we lack large- Δ objects at the latest times, while we still have a handful of SNe Ia with small Δ values at these epochs. This is unsurprising since objects with large Δ values are fainter and have faster-evolving light curves, and thus we are not able to follow them spectroscopically for as long as their small- Δ brethren. It is interesting to note that there are relatively few SNe Ia with $0.5 \leq \Delta \leq 0.7$ or $1.1 \leq \Delta \leq 1.3$; these possible anomalies will be investigated further in future BSNIP papers.

6.2 Object (Re-)Classification

Some of the SNe Ia presented here were originally classified as other types of SNe or remained unclassified prior to this work. Using our SNID classification scheme we have reclassified these objects as bona fide SNe Ia. Similarly, there are a few objects in our dataset that, again after applying our spectral classification procedure, were found to be examples of some of the peculiar SN Ia subtypes. All of the objects for which (re-)classifications were made are described below and plots of their spectra compared to their best-matching SNID template can be found online (see the Supporting Information).

6.2.1 SN 1991O

This SN was discovered on 1991 Mar. 18, by Mueller & Filippenko (1991), and classified as a SN Ia “about 1–2 months past maximum brightness” (Mueller & Filippenko 1991).

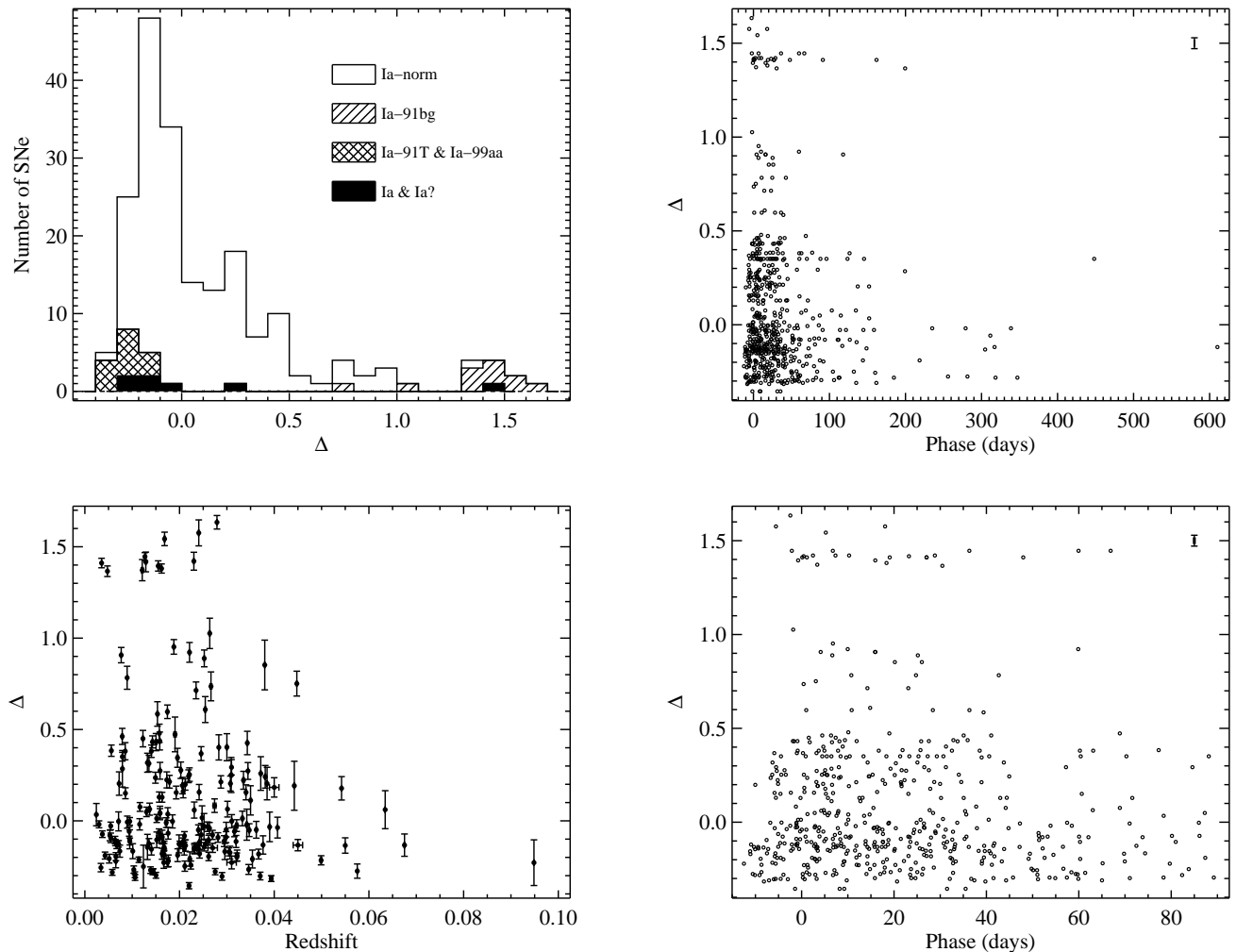


Figure 11. A histogram of the MLCS2k2 Δ value (which is a measurement of the light-curve shape) of each SN Ia (for which we have light-curve shape information, *top left*). Our average Δ is about 0.12 and our median Δ and uncertainty is about -0.03 and 0.035 . The different shadings correspond to each object’s final SNID classification (Section 5.4.2). The host-galaxy redshift versus the MLCS2k2 Δ value of each SN Ia (for which we have light-curve shape information, *bottom left*). The phase versus the MLCS2k2 Δ value of each spectrum for which we have light-curve shape information (*top right*) and a zoom-in on those spectra with $t \leq 90$ d (*bottom right*). The median error bar in both directions is shown in the top-right corner of each of these two panels.

Our SNID classification reveals that SN 1991O is 91bg-like, most similar to SN 2006em ~ 21 d past maximum brightness.

6.2.2 SN 1993aa

This SN was discovered on 1993 Sep. 19, by Pollas et al. (1993), and classified as a SN Ia “probably about 1 month past maximum brightness” (Pollas et al. 1993). Our SNID classification reveals that SN 1993aa is also 91bg-like, most similar to SN 2007ba ~ 8 d past maximum brightness.

6.2.3 SN 1998cm

This SN was discovered on 1998 Jun. 10, by Germany et al. (1998), and classified as a SN Ia “within a week or two of maximum brightness” (Germany et al. 1998). Our SNID classification reveals that SN 1998cm is 91T-like, most similar to SN 1997br ~ 8 d past maximum brightness.

6.2.4 SN 2000J

This SN was discovered on 2000 Feb. 4, by Puckett et al. (2000). Nearly 6 weeks later it was classified as a SN II based on the noisy spectrum presented in this work (Filippenko & Coil 2000). However, a SNID fit to the same spectrum reveals that it is more likely a normal SN Ia, most similar to SN 1994D ~ 54 d past maximum brightness.

6.2.5 SN 2001es

This SN was discovered on 2001 Oct. 7, by Li (2001), but it has remained unclassified until now. From a SNID fit to one of the spectra presented in this work, we determine that it is likely a normal SN Ia, most similar to SN 2004fz ~ 22 d past maximum brightness.

6.2.6 SN 2002bp

This SN was discovered on 2002 Mar. 8, by Puckett & Languoussis (2002), but it too has remained unclassified until now. From a SNID fit to our spectrum presented here, we determine that it is a SN 2002cx-like object. Upon further inspection, it seems to be a better match to the quite peculiar SN 2008ha (Foley et al. 2009a) than to the more “normal” members of the SN 2002cx-like class (e.g., Jha et al. 2006). We include SNe 2002bp and 2008ha here in our SN Ia sample even though there is uncertainty regarding whether SN 2008ha was in fact a SN Ia (e.g., Valenti et al. 2009).

6.2.7 SN 2004br

This SN was discovered on 2004 May 15, by Graham & Foley (2004), and classified as “an unusual type Ia supernova, similar to the spectrum of SN 2000cx” (Gerardy et al. 2004). The SNID classification of our earliest spectrum of SN 2004br reveals that it is likely 99aa-like, most similar to SN 2008ds ~ 5 d before maximum brightness. We are unable to confidently determine the subtype of the two older (both > 2 weeks past maximum brightness) spectra of SN 2004br in our dataset. The best-matching template of one of these other spectra is another 99aa-like SN, and the best-matching template of the other is a 91T-like SN. Furthermore, Ganeshalingam et al. (in prep.) have determined that the MLCS2k2 Δ parameter of SN 2004br is -0.152 . This spectral and photometric information increases our confidence in the 99aa-like classification of SN 2004br, though it is still uncertain.

6.2.8 SN 2005dh

This SN was discovered on 2005 Aug. 10, by Moore & Li (2005), and classified as a SN Ia “near maximum light” (Salvo et al. 2005). The SNID classifications of both spectra of SN 2005dh in our sample reveal it to be 91bg-like with the earlier spectrum being most similar to SN 2006cs ~ 2 d past maximum brightness. This object was specifically noted to have an “unusually high” expansion velocity of $16,000\text{--}16,600 \text{ km s}^{-1}$ (based on the minimum of the Si II $\lambda 6355$ absorption feature; Salvo et al. 2005; Gal-Yam et al. 2005). However, both Salvo et al. (2005) and Gal-Yam et al. (2005) used the host-galaxy redshift presented by Falco et al. (1999), $z = 0.038$, as opposed to the actual host-galaxy redshift of $z = 0.015$ (Adelman-McCarthy et al. 2008). Using the correct redshift, we calculate a relatively normal expansion velocity of $\sim 9300 \text{ km s}^{-1}$ for our spectrum of SN 2005dh from a similar epoch.

6.2.9 SN 2008Z

This SN was discovered on 2008 Feb. 7, by Puckett et al. (2008), and classified as a Type Ia (Blondin & Calkins 2008). The SNID classification of our earliest spectrum of SN 2008Z reveals that it is 99aa-like, most similar to SN 2008ds at maximum brightness. Ganeshalingam et al. (in prep.) have determined that the MLCS2k2 Δ parameter of SN 2008Z is -0.152 .

6.2.10 SN 2008ai

This SN was discovered on 2008 Feb. 13, by Boles & Li (2008), and classified as a Type Ia (Silverman et al. 2008) using the earliest spectrum of this object presented here. Our SNID classification of this same spectrum reveals that it is actually 91bg-like, most similar to SN 2007ba ~ 5 d past maximum brightness.

6.3 New Redshifts for Individual Objects

Some of the objects in our dataset do not have published spectroscopic host-galaxy redshifts. Therefore, we have obtained host-galaxy spectra of several SNe presented in this work in order to determine their redshift. Furthermore, we have calculated the host-galaxy redshift of one of these objects with no published redshift based on narrow features present in our SN spectra. The SNe for which this was done, their host galaxies, the redshifts themselves, and basic information about the spectrum from which the redshift was determined can be found in Table 11. These redshifts are also listed in Table 1.

All of the spectra referred to in Table 11 were obtained from either Lick or Keck Observatory with the exception of the spectrum of the host of SN 2003ah. On 2008 Dec. 28, we obtained a 900 s medium-resolution spectrum of the host galaxy of SN 2003ah with the MagE spectrograph (Marshall et al. 2008) on the Magellan Clay 6.5 m telescope. Data reduction was similar to the process described in Section 3 with the exception of sky subtraction. For this spectrum, the sky was subtracted from the images using the method described by Kelson (2003). Further details of MagE data reduction are described in Foley et al. (2009a).

Two other objects in the BSNIP sample which lack published spectroscopic host-galaxy redshifts also deserve special mention. SN 2001ei was discovered in a faint host (LOTOS J235102.95+271050.6) with no known redshift (Martin & Li 2001); however it is likely within the Abell 2666 galaxy cluster ($cz \approx 8040 \text{ km s}^{-1}$), possibly associated with NGC 7768 ($cz \approx 8190 \text{ km s}^{-1}$). These redshifts are slightly lower than the SNID-determined redshifts for our two spectra of SN 2001ei (as listed in Table 7). SN 2004fy was discovered in MCG +15-1-10, which is probably interacting with NGC 3172 ($cz \approx 6100 \text{ km s}^{-1}$). This matches well with the SNID-determined redshift for one of our spectra of SN 2004fy, though it is somewhat larger than that of the other spectrum. Due to the uncertainty of both of these objects’ host redshifts, they are not listed in Table 1.

7 CONCLUSION

In this first BSNIP paper we presented a large, homogeneous set of low-redshift ($z \leq 0.2$) optical spectra of SNe Ia. 584 spectra of 199 SNe have well-calibrated light curves with measured distance moduli, and many of the spectra have had host-galaxy corrections applied. We also discussed our observing and reduction procedures used during the two decades over which we collected these data, as well as our “colour matching” method for removing residual galaxy contamination. Our relative spectrophotometry was shown to be extremely accurate for the vast majority of our dataset.

Table 11. Previously Unpublished Spectroscopic Host-Galaxy Redshifts

SN Name	Host Galaxy	cz_{helio} (km s ⁻¹) ^a	UT Date of Spectrum ^b	SN/Gal ^c	Abs/Emis ^d
SN 2003ah	LOTOSS J044309.01+004553.4	10153 (3)	2008-12-28	Gal	Emis
SN 2006mp	MCG +08-31-29	8090 (300)	2006-11-03	Gal	Emis
SN 2008s3 ^e	2MASX J23004648+0734590	12300 (300)	2008-09-08	Gal	Abs
SN 2008s5 ^f	...	9290 (300)	2008-09-22	SN	Emis

^aThe redshift uncertainty is in parentheses.
^bUT date of the spectrum from which we determined the redshift.
^c“Gal” = Spectrum from which we determined the redshift was of the host galaxy itself; “SN” = Spectrum from which we determined the redshift was of the SN but contained narrow host-galaxy spectral features.
^d“Emis” = Emission features were used to determine the redshift; “Abs” = Absorption features were used to determine the redshift.
^eAlso known as SNF20080825-006.
^fAlso known as SNF20080909-030.

How the data are currently stored and will eventually be made accessible to the astronomical community was also discussed.

In addition, we described the construction of our own set of SNID spectral templates as well as our classification scheme which utilises these new templates. Using our classification procedure we were able to classify for the first time (as well as reclassify) a handful of objects as bona fide SNe Ia. Furthermore, we presented classifications of objects as members of some of the peculiar SN Ia subtypes that were heretofore assumed to be “normal.” In total our dataset includes spectra of nearly 90 spectroscopically peculiar SNe Ia. We also determined spectroscopic host-galaxy redshifts of some objects where these values were previously unknown.

The sheer size of the BSNIP sample and the consistency of our observation and reduction methods makes this sample unique among all other published SN Ia datasets. In future BSNIP papers we will use these data to examine the relationships between spectroscopic characteristics and other observables (such as photometric and host-galaxy properties).

Our sample is also a preview of coming attractions; new large transient searches such as the Palomar Transient Factory (PTF; Rau et al. 2009; Law et al. 2009) and Pan-STARRS (Kaiser et al. 2002) will compile datasets similar in size to ours in just a few years.

ACKNOWLEDGMENTS

We would like to thank K. Alatalo, L. Armus, M. Baker, M. Bentz, E. Berger, M. Bershady, A. Blum, A. Burgasser, N. Butler, G. Canalizo, H. Chen, M. Cooper, C. DeBreuck, M. Dickinson, R. Eastman, M. Eracleous, S. Faber, X. Fan, C. Fassnacht, P. Garnavich, M. George, D. Gilbank, A. Gilbert, K. Glazebrook, J. Graham, G. Graves, R. Green, J. Greene, M. Gregg, M. Hidas, K. Hiner, W. Ho, J. Hoffman, I. Hook, D. Hutchings, V. Junkkarinen, L. Kewley, R. Kirshner, D. Kocevski, S. Kulkarni, M. Lehnert, B. Leibundgut, M. Malkan, A. Martel, M. McCourt, A. Miller, E. Moran, P. Nandra, J. Newman, K. Noeske, C. Papovich,

C. Peng, S. Perlmutter, M. Phillips, D. Pooley, H. Pugh, E. Quataert, M. Rich, M. Richmond, A. Riess, S. Rodney, K. Sandstrom, W. Sargent, K. Shimasaki, R. Simcoe, T. Small, G. Smith, H. Smith, H. Spinrad, G. Squires, C. Steidel, D. Stern, D. Stevens, R. Street, C. Thornton, T. Treu, B. Tucker, D. Tytler, W. van Breugel, V. Virgilio, V. Viscomi, N. Vogt, J. Walsh, D. Weisz, C. Willmer, A. Wolfe, and J.-H. Woo for their assistance with some of the observations over the last two decades. We would also like to thank J. Choi, M. Ellison, L. Jewett, A. Morton, X. Parisky, and P. Thrasher for helping to verify some of the information in the SNDB. Moreover, we thank the referee for comments and suggestions that improved the manuscript. We are grateful to the staffs at the Lick and Keck Observatories for their support. Some of the data presented herein were obtained at the W. M. Keck Observatory, which is operated as a scientific partnership among the California Institute of Technology, the University of California, and the National Aeronautics and Space Administration (NASA); the observatory was made possible by the generous financial support of the W. M. Keck Foundation. The authors wish to recognise and acknowledge the very significant cultural role and reverence that the summit of Mauna Kea has always had within the indigenous Hawaiian community; we are most fortunate to have the opportunity to conduct observations from this mountain. This research has made use of the NASA/IPAC Extragalactic Data base (NED) which is operated by the Jet Propulsion Laboratory, California Institute of Technology, under contract with NASA. A.V.F.’s group is supported by the NSF grant AST-0908886, DOE grants DE-FC02-06ER41453 (SciDAC) and DE-FG02-08ER41563, and the TABASGO Foundation. M.M. acknowledges support from Hubble Fellowship grant HST-HF-51277.01-A, awarded by STScI, which is operated by AURA under NASA contract NAS5-26555, for the time during which some of this work was conducted. KAIT and its ongoing operation were made possible by donations from Sun Microsystems, Inc., the Hewlett-Packard Company, AutoScope Corporation, Lick Observatory, the NSF, the University of California, the Sylvia & Jim Katzman Foundation and the TABASGO Foundation. We would like to ded-

icate this paper to the memory of Marc J. Staley, who never stopped asking the Great Questions.

REFERENCES

- Adelman-McCarthy J. K., et al., 2008, *ApJS*, 175, 297
Amanullah R., et al., 2010, *ApJ*, 716, 712
Astier P., et al., 2006, *A&A*, 447, 31
Bailey S., et al., 2009, *A&A*, 500, L17
Bessell M. S., 1990, *PASP*, 102, 1181
Blanton M. R., et al., 2003, *AJ*, 125, 2348
Blanton M. R., Roweis S., 2007, *AJ*, 133, 734
Blondin S., Calkins M., 2008, *CBET*, 1246, 1
Blondin S., et al., 2008, *ApJ*, 682, 724
Blondin S., et al., 2012, *AJ*, 143, 126
Blondin S., Mandel K. S., Kirshner R. P., 2011, *A&A*, 526, A81
Blondin S., Tonry J. L., 2007, *ApJ*, 666, 1024
Boles T., Li W., 2008, *CBET*, 1256, 1
Brahe T., 1573, *De Nova Stella*
Cardelli J. A., Clayton G. C., Mathis J. S., 1989, *ApJ*, 345, 245
Colgate S. A., McKee C., 1969, *ApJ*, 157, 623
Conley A., et al., 2011, *ApJS*, 192, 1
Contreras C., et al., 2010, *AJ*, 139, 519
Cooper M. C., Newman J. A., Davis M., Finkbeiner D. P., Gerke B. F., 2012, in *Astrophysics Source Code Library*, record ascl:1203.003 spec2d: DEEP2 DEIMOS Spectral Pipeline. p. 3003
Ellis R. S., et al., 2008, *ApJ*, 674, 51
Faber S. M., et al., 2003, in Iye M., Moorwood A. F. M., eds, *Proceedings of the Society of Photo-Optical Instrumentation Engineers (SPIE) Conference*. Vol. 4841. p. 1657
Falco E. E., et al., 1999, *PASP*, 111, 438
Filippenko A. V., 1982, *PASP*, 94, 715
Filippenko A. V., 1988, *AJ*, 96, 1941
Filippenko A. V., 1997, *ARA&A*, 35, 309
Filippenko A. V., Coil A. L., 2000, *IAU Circ.*, 7381
Filippenko A. V., Li W. D., Treffers R. R., Modjaz M., 2001, in Paczyński B., Chen W. P., Lemme C., eds, *Small-Telescope Astronomy on Global Scales. The Lick Observatory Supernova Search with the Katzman Automatic Imaging Telescope*. *Astron. Soc. Pac.*, San Francisco, p. 121
Filippenko A. V., Matheson T., Ho L. C., 1993, *ApJ*, 415, L103
Foley R. J., et al., 2003, *PASP*, 115, 1220
Foley R. J., et al., 2009a, *AJ*, 138, 376
Foley R. J., et al., 2009b, *AJ*, 137, 3731
Foley R. J., et al., 2012, *AJ*, 143, 113
Foley R. J., Filippenko A. V., Leonard D. C., Riess A. G., Nugent P., Perlmutter S., 2005, *ApJ*, 626, L11
Foley R. J., Kasen D., 2011, *ApJ*, 729, 55
Foley R. J., Smith N., Ganeshalingam M., Li W., Chornock R., Filippenko A. V., 2007, *ApJ*, 657, L105
Gal-Yam A., Sand D., Leonard D., 2005, *The Astronomer's Telegram*, 581, 1
Ganeshalingam M., et al., 2010, *ApJS*, 190, 418
Garavini G., et al., 2004, *AJ*, 128, 387
Gerardy C. L., Roman B., Deglman F., 2004, *IAU Circ.*, 8343, 3
Germany L., Sabine S., Chan S., Filippenko A. V., Leonard D. C., Modjaz M., Eastman R. G., 1998, *IAU Circ.*, 6943, 2
Graham J., Foley R. J., 2004, *IAU Circ.*, 8340, 1
Guy J., Astier P., Nobili S., Regnault N., Pain R., 2005, *A&A*, 443, 781
Guy J., et al., 2007, *A&A*, 466, 11
Hamuy M., et al., 1996, *AJ*, 112, 2408
Hicken M., et al., 2009, *ApJ*, 700, 331
Hicken M., Wood-Vasey W. M., Blondin S., Challis P., Jha S., Kelly P. L., Rest A., Kirshner R. P., 2009, *ApJ*, 700, 1097
Hillebrandt W., Niemeyer J. C., 2000, *ARA&A*, 38, 191
Ho W. C. G., Van Dyk S. D., Peng C. Y., Filippenko A. V., Leonard D. C., Matheson T., Treffers R. R., Richmond M. W., 2001, *PASP*, 113, 1349
Horne K., 1986, *PASP*, 98, 609
Hoyle F., Fowler W. A., 1960, *ApJ*, 132, 565
Ilbert O., et al., 2006, *A&A*, 457, 841
Jha S., Branch D., Chornock R., Foley R. J., Li W., Swift B. J., Casebeer D., Filippenko A. V., 2006, *AJ*, 132, 189
Jha S., et al., 2006, *AJ*, 131, 527
Jha S., Riess A. G., Kirshner R. P., 2007, *ApJ*, 659, 122
Kaiser N., et al., 2002, in Tyson J. A., Wolff S., eds, *Proceedings of the Society of Photo-Optical Instrumentation Engineers (SPIE) Conference*. Vol. 4836. p. 154
Kelson D. D., 2003, *PASP*, 115, 688
Kessler R., et al., 2009, *ApJS*, 185, 32
Kimeridze G. N., Tsvetkov D. Y., 1991, *AZh*, 68, 341
Law N. M., et al., 2009, *PASP*, 121, 1395
Leonard D. C., et al., 2002, *PASP*, 114, 35
Li W., 2001, *IAU Circ.*, 7729
Li W., et al., 2001, *PASP*, 113, 1178
Li W., et al., 2003, *PASP*, 115, 453
Li W., et al., 2011, *MNRAS*, 412, 1441
Li W., Filippenko A. V., Riess A. G., 2001, *ApJ*, 546, 719
Li W., Filippenko A. V., Treffers R. R., Riess A. G., Hu J., Qiu Y., 2001, *ApJ*, 546, 734
Marshall J. L., et al., 2008, in *Society of Photo-Optical Instrumentation Engineers (SPIE) Conference Series* Vol. 7014 of *Society of Photo-Optical Instrumentation Engineers (SPIE) Conference Series*, The MagE spectrograph
Martin P., Li W. D., 2001, *IAU Circ.*, 7718, 1
Matheson T., et al., 2005, *AJ*, 129, 2352
Matheson T., et al., 2008, *AJ*, 135, 1598
Matheson T., Filippenko A. V., Ho L. C., Barth A. J., Leonard D. C., 2000, *AJ*, 120, 1499
Matheson T., Filippenko A. V., Li W., Leonard D. C., Shields J. C., 2001, *AJ*, 121, 1648
Miknaitis G., et al., 2007, *ApJ*, 666, 674
Miller J. S., Stone R. P. S., 1987, *Lick Obs. Tech. Rep.* 48. Santa Cruz: Lick Obs.
Miller J. S., Stone R. P. S., 1993, *Lick Obs. Tech. Rep.* 66. Santa Cruz: Lick Obs.
Moore M., Li W., 2005, *CBET*, 196, 1
Mueller J., Filippenko A. V., 1991, *IAU Circ.*, 5233, 1
Mulchaey J., Gladders M., 2005, *LDSS-3 User's Guide*. The Carnegie Observatories, Pasadena

- Newman J. A., et al., 2012, ApJS, submitted (arXiv:1203.3192)
- Nomoto K., Thielemann F.-K., Yokoi K., 1984, ApJ, 286, 644
- O'Donnell J. E., 1994, ApJ, 422, 158
- Oke J. B., 1990, AJ, 99, 1621
- Oke J. B., Cohen J. G., Carr M., et al., 1995, PASP, 107, 375
- Oke J. B., Gunn J. E., 1982, PASP, 94, 586
- Oke J. B., Gunn J. E., 1983, ApJ, 266, 713
- Östman L., et al., 2011, A&A, 526, A28
- Peek J. E. G., Graves G. J., 2010, ApJ, 719, 415
- Perlmutter S., et al., 1999, ApJ, 517, 565
- Phillips A. C., Miller J., Cowley D., Wallace V., 2006, in Proceedings of the Society of Photo-Optical Instrumentation Engineers (SPIE) Conference. Vol. 6269. p. 56
- Phillips M. M., 1993, ApJ, 413, L105
- Pollas C., Filippenko A. V., Matheson T., 1993, IAU Circ., 5871, 1
- Poznanski D., Gal-Yam A., Maoz D., Filippenko A. V., Leonard D. C., Matheson T., 2002, PASP, 114, 833
- Puckett T., Gagliano R., Orff T., 2008, CBET, 1241, 1
- Puckett T., George D., Rest A., Krisciunas K., 2000, IAU Circ., 7362
- Puckett T., Langoussis A., 2002, IAU Circ., 7847
- Rau A., et al., 2009, PASP, 121, 1334
- Riess A. G., et al., 1997, AJ, 114, 722
- Riess A. G., et al., 1998, AJ, 116, 1009
- Riess A. G., et al., 1999, AJ, 117, 707
- Riess A. G., et al., 2007, ApJ, 659, 98
- Riess A. G., Press W. H., Kirshner R. P., 1996, ApJ, 473, 88
- Salvo M., Schmidt B., Davis T., Sankarankutty S., 2005, CBET, 199, 1
- Savitzky A., Golay M. J. E., 1964, Analytical Chemistry, 36, 1627
- Schlegel D. J., Finkbeiner D. P., Davis M., 1998, ApJ, 500, 525
- Sheinis A. I., Bolte M., Epps H. W., Kibrick R. I., Miller J. S., Radovan M. V., Bigelow B. C., Sutin B. M., 2002, PASP, 114, 851
- Silverman J. M., 2012, PhD thesis, University of California, Berkeley, Berkeley, California
- Silverman J. M., Steele T. N., Ganeshalingam M., Lee N., Filippenko A. V., 2008, CBET, 1264, 1
- Stritzinger M. D., et al., 2011, AJ, 142, 156
- Strolger L., et al., 2002, AJ, 124, 2905
- Sullivan M., et al., 2011, ApJ, 737, 102
- Suzuki N., et al., 2012, ApJ, 746, 85
- Tripp R., 1998, A&A, 331, 815
- Tsvetkov D. I., Volkov I. M., Bartunov O. S., Ikonnikova N. P., Kimeridze G. N., 1990, A&A, 236, 133
- Turatto M., 2003, in Weiler K., ed., Supernovae and Gamma-Ray Bursters. Springer-Verlag, Berlin, p. 21
- Valenti S., et al., 2009, Nature, 459, 674
- Wang X., et al., 2009, ApJ, 699, L139
- Wells L. A., et al., 1994, AJ, 108, 2233
- Wood-Vasey W. M., et al., 2007, ApJ, 666, 694